Published in final edited form as:
Wiley Interdiscip Rev Nanomed Nanobiotechnol. 2013 ; 5(6): 517–543. doi:10.1002/wnan.1231.

A Brief Account of Nanoparticle Contrast Agents for Photoacoustic Imaging

Dipanjan Pan[1], **Benjamin Kim**[1], **Lihong V. Wang**[2], and **Gregory M Lanza**[1]

[1]Department of Medicine, Washington University School of Medicine, St Louis, MO 63108

[2]Department of Biomedical Engineering, Washington University, St Louis, MO 63130

Abstract

Photoacoustic imaging (PAI) is a hybrid, nonionizing modality offering excellent spatial resolution, deep penetration, and high soft tissue contrast. In PAI, signal is generated based on the absorption of laser-generated optical energy by endogenous tissues or exogenous contrast agents leading to acoustic emissions detected by an ultrasound transducer. Research in this area over the years has shown that PAI has the ability to provide both physiological and molecular imaging, which can be viewed alone or used in a hybrid modality fashion to extend the anatomic and hemodynamic sensitivities of clinical ultrasound. PAI may be performed using inherent contrast afforded by light absorbing molecules such as hemoglobin, myoglobin, and melanin or exogenous small molecule contrast agent such as near infrared dyes and porphyrins. However, this review summarizes the potential of exogenous nanoparticle-based agents for PAI applications including contrast based on gold particles, carbon nanotubes, and encapsulated copper compounds.

Keywords

Photoacoustic imaging; gold nanoparticle; copper nanoparticle; carbon nanoparticle; NIR dyes; porphyrins; fibrin; angiogenesis; melanoma; sentinel lymphnode; thrombus

1. Introduction

Photoacoustic (PA) imaging, also referred to as optoacoustic imaging, is an emergent hybrid optical and ultrasound diagnostic modality with high spatial resolution and excellent soft tissue contrast. [1–6] In a typical photoacoustic system tissue is irradiated with a nonionizing short-pulsed laser beam within the acceptable the American National Standards Institute (ANSI) defined limits. [3] Endogenous proteins, e,g, hemoglobin, myoglobin, melanin, or exogenous PA contrast agents absorb the optical energy, undergo thermoelastic expansion, and produces photoacoustic (PA) waves that are received with a clinical or non-clinical, wide-band ultrasonic transducer (5–50 MHz). The PA images may be visualized alone or hybridized with an interleaved ultrasound image of the same field of interest. Because the PA image is created only from ultrasound generated within the tissue, it lacks

---

Address correspondence to: Dipanjan Pan, PhD, Assistant Professor in Medicine, Research, Division of Cardiology, Campus Box 8215, 660 Euclid Ave, Washington University School of Medicine, St. Louis, MO 63108, Tel: 314-454-7674, Fax: 314-454-5265, dpan@dom.wustl.edu.

the typical background speckle of ultrasound images. Moreover, PAI offers contrast sensitivity to physiological parameters such as the concentration and oxygenation of hemoglobin as well as unique molecular imaging contrast information.

While inherent PA contrast afforded by endogenous substances can be utilized for PA imaging to assess levels of vascularization and oxygen saturation in tumors [1–5], particularly malignant cancers, [7–8] a myriad of advances have been made in terms of exogenous contrast agent development for PA molecular imaging applications, particularly nanoparticle based technologies. As with inherent protein based contrast, the optical absorptive of exogenous agents dictates their utility for PA imaging. Several optically active materials have been explored as PA contrast agents, e.g. small molecule dyes, gold nanoparticles, single walled carbon nanotubes (SWNT), copper nanoparticles etc. [2, 9–10] However, given the optical absorptive capacity of blood and muscle, exogenous PA contrast enhancement must significantly exceed inherent background in vivo contrast. Moreover, these agents must have outstanding biocompatibility, appropriate in vivo stability (i.e., particularly during circulatory transit to targets and through the imaging period), and desirable synthetic processing attributes, specifically tolerance to sterilization and prolonged shelf-life stability. Although exogenous agents e.g. near infrared dye and porphyrin-based agents, has been administered directly into the blood pool, this review will focus on nanoparticulate compositions. (Figure 1) Examples of “nano”- contrast agents include different classes of gold nanoparticles of varying size and morphology (spherical vs. rod, cages); carbon nanotubes (SWNTs), hybrid nanoparticles (gold coated SWNTs) and copper oleate encapsulated nanoparticles.

2. Nanoparticle-based contrast agents

2.1. Gold Nanoparticles

Gold nanoparticles are excitable in the near-infrared (NIR) range within the “optical transmission window” of biological tissues (λ = 650–900 nm). This allows for deeper light penetration, lower autofluorescence, and reduced light scattering. In addition to strong optical absorption, gold particles, unlike small molecule fluorophores, are resistant to photobleaching or fading due to dye destruction. [11–13] Gold nanoparticles exhibit a phenomena known as localized surface plasmon resonance (LSPR) due to their inherent abilities to absorb and scatter light at specific wavelengths. Nanoparticle LSPR refers to the resonance established when incident light photons match frequency of particle surface electrons vibrating against the opposing restoring force of positive nuclei. LSPR can be manipulated by altering particle shape and surface coating. Several possibilities of PA contrast imaging involving gold nanoparticles have been explored by multiple research groups.

Gold nanocages as photoacoustic contrast agents—The LSPR of gold nanoparticles typically must be tuned from the visible electromagnetic range of energies, where blood and tissue attenuation impairs light penetration, into the near-infrared region (NIR) bandwidth for maximum interrogation depth *in vivo*. This is the so-called NIR window. Conventional spherical gold particles does places the LSPR in the visible light realm, which led Younan Xia and co-workers to embark upon development of a novel class of nanoparticles called gold nanocages (AuNC). These particles were characterized by hollow interiors enclosed by a singlecrystal ultrathin outer structure with porous walls. [14] Xia demonstrated that these AuNCs exhibited wavelength plasticity and could be manipulated to any wavelength in the NIR region based on their modifications of the nanocage sizes and thickness. Additionally, due to their novel properties, which included high absorption, low cytotoxicity, and their ability to be easily conjugated to tumor-specific ligands, AuNCs provided highly effective PA contrast imaging. [15–17]

Golf nanocage synthesis: AuNCs synthesis followed a galvanic replacement reaction using Ag solid as a template for the reduction of $HAuCl_4$ due to their electrochemical potential difference to form Au atoms. In this reaction, the growth of AuNCs is template over silver nanocubes that are concurrently produced.

$$3\mathrm{Ag(s)}+\mathrm{AuCl}_4^-(\mathrm{aq})-->\mathrm{Au(s)}+3\mathrm{Ag}^+(\mathrm{aq})+4\mathrm{Cl}^-(\mathrm{aq})$$

Ag nanocubes were synthesized using $AgNO_3$ or CF_3COOAg as a precursor to Ag, and a polyol reduction by using ethylene glycol as a solvent and a source of reducing agent. This reaction was further assisted with a capping agent, poly(vinyl pyrrolidone) (PVP). Subsequently, the addition of catalytic amounts of NaHS and or Cl^- ions imparted rapid nucleation of single-crystal seeds while simultaneously, due to oxidative etching, discarded twinned seeds, and ultimately formed single-crystal Ag nanocubes. Additional titration of these Ag nanocubes with $HAuCl_4$ was followed at 100°C in order to ensure maximal growth of thin layered Au on the surface of the Ag crystals and to evade precipitation of AgCl. Cooling the reaction precipitates AgCl, which is then dissolved in a saturated NaCl solution and eliminated, leaving AuNCs as the final remaining product. (Figure 2) Interestingly, the formation of AuNCs can be distinctively noted by observing the extinction spectra of the titration of Ag nanocubes with varying volumes of $HAuCl_4$. As more $HAuCl_4$ is added to the Ag nanocubes to promote epitaxial growth of AuNCs, the LSPR peak shifts from the visible light into the NIR region.

PA imaging of cerebral cortex via AuNC: The cranium and cerebral cortex of rodent lend themselves to photoacoustic techniques, being permeable to laser light and ultrasonic RF waves. [18–20] Wang et al. [21] imaged of the vasculature blood pool in rat brain using gold nanoshells with >100 nm diameters that was further improved in collaboration with Xia et al. [22] utilizing smaller AuNCs (<50 nm). Figure 3 shows the comparative results of an *ex vivo* photoacoustic study produced from pure rat blood and a mixture of AuNC-rat blood, and an in vivo study of injections of AuNCs in the cerebral cortex of a rat model. *Reproduced with permission from (21)*

Sentinel lymph node mapping via AuNCs: Sentinel lymph node (SLN) imaging is an adjunctive technique used with minimally invasive breast cancer surgery, or lumpectomy, to guide SLN identification and resection for disease staging and prognosis. [23–28] Typically, methylene blue dye or radioactive colloid are utilized to preoperatively localize the SLN. However, despite its widely used practice, radioactive colloids have low precision and difficulty in localization due to very low lateral and negligible vertical resolution, which can accrue to potentially harmful effects when resecting the SLN during surgical operations. On the other hand, methylene blue stain can be difficult to place preoperatively or detect intraoperative, offering far less sensitivity than the nuclear counterpart. Besides the imprecision of SLN methylene blue technique, potential adverse effects including allergic reactions are frequent with the stain. [29]

Xia and co workers demonstrated that AuNCs can be injected subcutaneously, migrate to the draining lymphnode to afford effective sentinel lymph node mapping [30] with high spatial resolution at imaging depths reaching 33 mm. (Figure 4)

Imaging melanoma with AuNCs: AuNCs can be surface modified with functional, biologically relevant moieties, AuNC's surface groups were modified with thiol-PEG groups and then conjugated to [Nle^4,D-Phe^7]-*a*-melanocyte-stimulating hormone ([Nle^4,D-Phe^7]-*a*-MSH). [31] The homing ligand, [Nle^4,D-Phe^7]-*a*-MSH, has the ability to bind to *a*-MSH receptors over-expressed on melanomas, thus acting as a method to retain and concentratie these particles at the tumor site. Photoacoustic signals increased significantly with time as shown in Figure 5 and 6 for the targeted [Nle^4,D-Phe^7]-*a*-MSH-AuNCs when compared with nontargeted AuNC, resulting in almost 300% PA signal enhancement. These results suggested that the MSH-targeted AuNCs were undergoing ligand-receptor binding with the melanoma cells and suggested further efficacy and applicability for ligand-modified AuNCs.

2.2 Carbon nanotubes for advanced contrast agents

Because carbon nanotubes (CNT) are strongly optically active over a wide range of wavelengths relevant to PA imaging, many studies were devoted to exploring the potential of CNTs for PA applications. Following the work of Zharov *et. al* [32] who initially demonstrated the potential of CNTs to function as exogenous PA contrast agents, others have extended this result by coupling targeting peptides containing an RGD (arginine-glycine-aspartate) motif to the tumor neovasculature in mice [33]. Additional modifications of CNT chemistry and coating for enhancement of contrast [34–36] led to their use for SLN mapping and tumor cell characterization [36–41]. Interestingly, CNTs also found utility for therapeutic hyperthermia application, which was demonstrated in vitro with tumor and bacterial cells [42–50].

2.3 CNT hybrids

Unfortunately, CNTs have a relatively low NIR absorption coefficient compared with gold nanoparticles, [49] and therefore require very high local concentrations to produce useful PA contrast imaging. [35–36] Single-walled nanotube (SWNT) have a very high surface area (~1300 m^2/g) for interacting with optical radiation. To enhance this, a hybrid gold-SWNT was devised wherein the SWNT core coated with a gold layer (SWNT-Au) [36] (Figure 7b). The hybrid SWNT-Au offered a more biocompatible surface that was better for chemical bioconjugation of homing ligands or drugs. Compared with SWNT alone, the gold layer greatly augmented LSPR the responses of the SWNT-Au hybrids.

An alternative approach to the low NIR absorption properties of SWNT was achieved by coupling small molecule dyes onto the high surface area of the nanotubes. Liu *et. al.* [51]

demonstrated this effect by loading indocyanine green (ICG) molecules onto SWNTs via simple pi-pi bond stacking of hydrophobic benzene rings. Remarkably, hybrid ICG-SWNTs exhibited a 20-fold increase in optical absorption (Figure 7c)

Applications of CNT geared towards photoacoustic imaging—SWNT were used to enhance contrast from the neovasculature by coupling RGD peptides via a PL-PEG$_{5400}$ [52]. Integrin-targeted SWNTs' were evaluated in mice bearing U87 gliobastoma xenograft tumors and showed a significantly higher PA signal (~7-fold increase) in the tumor compared to that of the untargeted SWNTs (Figure 8).

To further enhance SWNT-RGD contrast, ICG, a small molecule optical dye, was hydrophobically coupled to the surface structure. *In vitro* testing of SWNT-ICG-RGD constructs had stability in serum and a 300-fold increase in PA contrast associated with a shift in the laser excitation wavelength from 690 nm to 780 nm when compared to SWNT-RGD. However, despite the photoresistive nature of SWNT particles, photobleaching was observed in the cyanine dye modified version. This optical fading of PA contrast reflected the optical instability of ICG rather than structural degradation of the SWNT. In vivo, SWNT-ICG-RGD were shown to target tumor neovasculature. (Figure 9) [34]

Hybrid Magnetic/Gold nanoparticles—Development of techniques to assay and characterize circulating tumor cells (CTCs) are emerging as an area of Nanomedicine research. Unfortunately such assays are limited by sampling errors, which relates to the probability that adequate numbers of cancer cells are contained with the minute blood volume measured. Typically, these methods have high sensitivities for detecting cells when present, but limited sample volume and sparse numbers of cells circulating, particularly in early stages of cancer, reduces the overall sensitivity of the method. One approach to address the issue has been the development of multiplex targeting strategy utilizing a conjugated nanoparticle consisting of a magnetic (MNP) and gold nanoparticle (GNP) which have the properties of having an absorption spectra in the NIR region and allows for detection of two colors at laser wavelengths of 639 and 900 nm as shown in Figure 10 A, B. These conjugated nanoparticles were specifically synthesized to evade normal blood cells, and to specifically target urokinase plasminogen activator (ATF) and folate receptors. [35] PA signals indicated that the optimal NP concentration and solution volume were 10^9 NPs/ml for GNTs and 10–20 μl respectively. Also, there were no detectable PA signals in mouse ear microvessels above blood background which suggested that PA signals were able to differentiate between bound and unbound NPs, supporting its specificity. In order to detect CTCs in a primary tumor, photoacoustic flow cytometry (PAFC) was used to measure the progressive increase in the number of CTCs over a course of four weeks, and showed a high correlation with respect to the progression of the tumor (Figure 10C,D). Such method deemed as '*in vivo* blood cancer test,' proves as an applicable and potential measure for early PA diagnosis of primary tumors and prevention of metastasis.

Gold nanobeacons: Gold nanobeacons (GNB) were developed by entrapping numerous small gold nanoparticles (spherical, 2–4 nm) within a larger colloidal particle, encapsulated with a biocompatible phospholipids coating in our laboratories. (53–56) It was presumed that the entrapment of numerous small gold particles would greatly amplify the signal for each binding event, effectively similar to a larger single gold particle, but upon particle metabolism, the gold particles, falling below the renal elimination threshold (6–10 nm), would be bioeliminated through the kidney and urine. Moreover, the interaction of the small particles within the matrix of the lipid encapsulated particle would lead to effectively creating a randomly irregular shapes that would shift the optical absorbance peak for visible into the NIR spectral region for optimal in vivo use.

The first generation gold nanobeacon (GNB_1) were synthesized by suspending octylthiol-coated spherical gold nanoparticles (AuNPs, 2 w/v%,) in vegetable oil (20 vol%) matrix followed by homogenization of the mixture with phospholipid surfactants mixture (2 w/v%) (Figure 11). The phospholipids mixture was comprised of phosphatidylcholine (PC, 91 mole %) and cholesterol (8 mole %) and included biotin-caproyl-PE (1 mole %) or a phospholipid anchored homing ligand (0.3 to 1.0 mole %) at the equimolar expense of PC dependent on the biological target under question. The GNB_1 particles were 154 ± 10 nm with polydispersity and zeta potential of 0.08 ± 0.03 and −47 ± 7 mV, respectively (Brookhaven Instrument Co.). Gold content, determined by ICP-MS, was 1080 μg/g of the 20% colloid suspension. UV-vis spectroscopy confirmed the absorbance at ~520 nm and in the near-infrared (NIR) window (~900 nm). GNB_1 particles exhibited remarkable stability as observed by the particle size and zeta potential, which varied <5% over 100 days when stored at 4°C under argon in sealed serum vials.

The PA signal from a 20% GNB suspension mixed 1:1 with rat blood within Tygon® tubing (I.D. 250 μm, O.D. 500 μm) was 15 times stronger than that from pure rat blood. [14] When monitored over the entire 740–820 nm NIR window, the average PA signal enhancement by GNB over blood was greater than 10-fold. (Figure 12) While the agent offered high contrast for typical blood pool applications, the intent of the agent was for vascular-targeted molecular imaging medical applications of clinical importance and unmet need, such as intravascular thrombosis, neovascularization in cancer and atherosclerosis, and inflammation in cancer, arthritis, and more. Detecting intravascular targets requires a substantial signal over the background contrast associated with circulating erythrocyte hemoglobin.

The initial target for GNB_1 was to detect fibrin in thrombosis as a means to diagnose ruptured carotid atherosclerotic plaques in patients at high risk for stroke. Today, ultrasound is used to assess carotid stenosis as clinical tool to guide medical decisions for surgical carotid endarterectomy (CEA) versus medical therapy alone. While patients with greater than 70% stenosis benefit from CEA, the vast majority of high risk individuals stroking over a two year period have less than 60% stenosis. In many patients with severe disease, small and repeated microruptures of the plaque intima with intermittent healing preceeds a major event. To minimize the financial and human costs of stroke, PA imaging could be added to standard diagnostic carotid imaging of high-risk patients as a technique to identify microthrombi in small endothelial microfissures, which could potentially support earlier surgical intervention and a greater reduction in stroke incidence.

As an initial proof of concept, GNB_1 and the control nanobeacons (i.e., containing no gold) were pretargeted to acellular fibrin clot phantoms with classic avidin-biotin coupling. The particles were homed to fibrin using a well-characterized biotinylated anti-human fibrin-specific monoclonal antibody (NIB5F3). [57] The clots were prepared in low-density polyethylene (LDPE) tube (~1 cc volume, I. D. ~6 mm) and treated with biotinylated GNB and control (targeted, no gold nanobeacon). Figures 12(E) and 12(F) show cross-sectional PAT images using a curved array PAT system [58] with an 800 nm wavelength laser. As evident from the images, high contrast was clearly appreciated for the clots targeted with biotinylated GNB_1 in comparison to the control clot.

The cross-sectional PAT images were obtained using a PA breast scanner system, [59] of the same control and targeted plasma clots, respectively [Figures 12(G) and 12(H)]. [53] Similar to the previous experiments, the targeted plasma clot was clearly distinguishable (Figure 12(F)) in the PAT image, whereas the control clot image was not appreciable (Figure 12(E)). This result was corroborated analytically by total gold content analyses using inductively couple plasmon resonance (ICP-MS). The total gold content of the clots with targeted GNB_1, nontargeted GNB_1 and targeted nonmetallic nanobeacons were found to be 47μg/g, not detected (ND, <0.02 μg/g) and ND respectively, by ICP-MS. This experiment, for the first time, clearly illustrated the concept of intravascular PA with GNB_1.

Gold nanobeacons (Rod) as alternative to spherical nanoparticles: Gold's optical properties can further be tuned and optimized to have more near infrared absorption. Rod-shaped gold nanoparticles (i.e., nanorods) offer distinct optical properties resulting from two surface plasmon (SP) bands corresponding to the transverse and longitudinal SP bands in the visible (λ = 520 nm) and the NIR (λ = 900 nm) regions, respectively. [11–13] Gold nanorods are frequently used as probes for fluorescence, light scattering, and two-photon luminescence imaging due to a large intrinsic extinction coefficient of the longitudinal band. The longitudinal SP bands are very sensitive to the aggregation of gold nanorods and the peak points of the SP bands predominantly depend on the anisotropic shape of each gold nanorod. The aggregation of rods generates isotropic (random) coupling of SP oscillations, and produces dramatic changes of the longitudinal SP bands. With these unique properties, gold nanorods interacting as a random cluster within a phospholipid encapsulated nanoparticle were expected to provide excellent contrast for photoacoustic imaging in the near-IR region.

The self-assembled gold nanobeacons (rods) [GNB_R] was based on the selfassembly of phospholipids in aqueous media to entrap multiple copies (i.e. hundreds) of gold atoms. [55] Parent gold nanorods (polymer coated GNR; transmission electron microscope axial diameter: 25 ± 5 nm, length: 80 ± 8 nm; lLSPR: 750nm, lTSPR: 530 nm) (Fig 13A) were dispersed in chloroform and premixed with vegetable oil (20% v/v almond oil) core matrix before encapsulated within phospholipids coating.

This synthesis resulted in an encapsulation of ~127 gold metal atoms (ICP-MS = 8.12 μg of gold/g of 20% colloidal nanobeacon), markedly less than GNB_1. The GNB_R particles had nominal hydrodynamic diameter of 129 ± 7 nm as measured by dynamic light scattering (DLS). The polydispersity and zeta potential were measured as 0.06 ± 0.02 and −41 ± 12 mV (Brookhaven Instrument Co.), respectively. The large negative zeta potential implied successful phospholipids encapsulation and high colloidal stability of these nanoparticles.

The dehydrated state diameter (D_{av}) and height parameters (H_{av}) of the GNB_R were 105 ± 28 and 60 ± 24 nm, as measured by transmission electron microscopy (TEM) and atomic force microscopy measurements (AFM), respectively (Figure 13B and 13C). Contrary to GNB_1 the encapsulation efficiency of the gold nanorods was low per GNB_R, which was anticipated due to the larger and irregular shape of the gold nanorods. Ultimately, GNB_R had less PA contrast relative to blood pool contrast (approximately 3-fold) and the larger gold nanorod size exceeded the renal threshold for bioelimination, bringing the issue of long-term safety in patients who would receive and likely retain these rods for life through out their bodies. With these results and concerns, subsequent studies from the group mainly utilized spherical gold nanoparticles similar to GNB_1.

Sentinel Lymphnode Imaging: As mentioned previously, breast cancer patients often undergo sentinel lymphnode biopsy (SLNB) in lieu of radical axillary dissection to exclude metastatic disease in patients undergoing lumpectomy. However, the technique can be complicated and the recovery of lymph nodes (LNs) is less adequate than expected and often the key tissue is missed. [60–61] Moreover, SLNB has been associated with post biopsy complications e.g. local seroma formation, lymphedema, nerve injury and numbness of arms. [62] In this context, efforts to improve noninvasive imaging of the axillary lymphnodes to guide minimally invasive percutaneous fineneedle biopsy (FNAB) or selective node resection for staging for breast cancer patients remains clinically relevant. Photoacoustics imaging offers marked advancements over typical preoperative methylene blue dye or radioactive labeling techniques to enhance intraoperative localization and resection. Contrast agents injected subcutaneously will migrate into lymphatics and travel to the sentinel LNs and can be detected at depths of 4 to 5 cm with PA imaging. In a series of studies, Pan et. al. demonstrated that the lymphatic transport of the nanopartculate contrast agents was highly influenced by size and mass.

The effectiveness of GNB_1 distribution into sentinel lymph node was studied first following a subcutaneous forepaw injection in a rodent model. [54] A sagittal maximum amplitude projection (MAP) photoacoustic image of the axillary area clearly delineated the vasculature by virtue of the light absorbing red blood cells with high spatial resolution of ~500 μm. Within 5 min, GNB_1 was found accumulated in the SLN and in adjacent secondary LN in the same chain. The signal clearly highlighted the lymphnode at this shallow depth, however, inorder to achieve a more robust contrast particularly for nodes farther from the transducer, further formulation approaches were considered and studied.

The most common, ´bigger is better´ mentality led to the development and evaluation of a larger PA agent with substantially more gold per particle than GNB_1. In this approach, GNB was a polymer encapsulated gold nanobeacon (GNB_P). In a typical synthesis of GNB_P, a diblock co polymer (polystyrene-b-polyacrylic acid) PS-*b*-PAA [63–66] ($Mn \times 10^3$: 0.8-*b*-29.3 PDI=1.18, 0.0033 mmoles) was dissolved in a mixture of methanol and $CHCl_3$ (4:1) and subjected to controlled evaporation under reduced pressure to generate a thin film of polymer. The thin film was dispersed in deionized water (0.2 μM) by probe sonication at ambient temperature. Octanethiol coated AuNPs (2w/v%) were suspended in polysorbate (sorbitan monolaureate (5 vol%) and microfluidized with PS-*b*-PAA dispersion (0.5 vol%) yielding a 10% colloidal suspension of nanoparticles (Figure 14). The nanobeacons were purified by exhaustive dialysis against infinite sink of nanopure water using cellulosic dialysis membrane (20 kDa MWCO). GNB_P (289 ± 24 nm) had a narrow distribution (polydispersity index: 0.15 ± 0.04). Following this approach, the gold content of GNB_1 (6120 metal atoms/particle) was impressively enhanced to reach 71,493 gold metal atoms per GNB_P. As expected, GNB_P produced very strong PA signal, which was significantly higher than GNB_1. [54]

However, contrary to our expectations, GNB_P was unable to provide signal enhancement in vivo. Injection of GNB_P into the rat forepaw followed by serial examination of the draining lymphnodes with PA imaging demonstrated no detectable signal over the anticipated course of the imaging session (Figure 6D). The LN territories of the animals were reimaged daily for the the next 3 days with no significant migration to and uptake of GNB_P by the sentinel lymphnode. Despite a tenfold increase in gold content and ultrahigh PA signal contrast in vitro, GNB_P was ineffective for in vivo LN imaging. We hypothesized that the larger size (and or mass) of GNB_P led to poor migration of the particles to and within the lymphatic channels, essentially leaving the contrast agents essentially at the injection site. Since bigger particles with more gold was ineffective, we explored the potential that a smaller particle with less gold, smaller size, and less mass would have better lymphatic migration. A third smaller gold nanobeacon (GNB_S), was produced and examined. [54]

GNB_S was prepared similar as GNB_1 by retuning the core matrix to polysorbates (Figure 14). Briefly, oleate-coated AuNPs (2 w/v% of inner matrix, 2–4 nm) were suspended in polysorbate (sorbitan monolaureate, 20 vol%) and homogenized with a surfactant mixture, resuspended from a lipid film, at 137.9 MPa (i.e., 20,000 PSI) for 4 min. The surfactant mixture was mainly comprised of phosphatidylcholine (PC) (92 mol% of lipid constitutents) and cholesterol (8 mole %). Hydrodynamic particle size for GNB_S was 92 ± 12 nm with a polydispersity index of 0.35 ± 0.05. The zeta potential (ζ) was −35 ± 8 nm, confirming appropriate particle encapsulation. Gold metal atom (9 gold metal atoms per GNB_S) content per particle was determined to be much less in comparison to GNB_1 and GNB_P. The result with GNB_S was dramatically improved relative to GNB_1 and GNB_p.

In the rat sentinel lymph node model, the blood-filled microvasculature was clearly visible (marked with red arrows) while the lymph node, devoid of optical absorbers, was not seen at baseline as before. Figure 6F and 6G present two MAP images of the same axillary area 5 min and 20 min after GNB-S subcutaneous injection into the mouse forepaw, respectively. The SLN is dramatically apparent as a bright spot (green arrow) and the conspicuity of the lymph node far exceeds what achieved previously with GNB_1 or GNB_p. GNB_S flowing within the lymphatic vessel toward and into the sentinal lymphnode was observed at 5 min post injection. Within 10 mins post GNB_S injection, the nanobeacons completed migration into LN and a persistent and robust signal was appreciated over the next hour. The contrast of the sentinel LN to the surrounding blood vessel was calculated to be 9:1 (ratio of the peak-to-peak PA signal amplitude obtained from blood vessel and SLN) after GNB_S injection. [54] In summary, the smaller GNB_S, with less gold particles per nanoparticle, less mass, and smaller size were more effective in detecting the SLN in comparison to the larger GNB particles. Moreover, the particles were retained adequately in the LN for practical use.

Integrin-specific photoacoustic imaging of angiogenesis: Angiogenesis is an essential process to expand the vasculature during embryonic development and adult life. In many inflammation related diseases, the angiogenic neovasculature is a microanatomical feature of medically important diseases, including cancer, atherosclerosis, and arthritis to name a few. Neovascularization reflects a multitude of pathologic processes that include cytokine liberation by inflammatory cells to stimulate endothelial proliferation, neovessel sprouting and microvessel development, as well as the secretion of matrix dissolving enzymes, such as metalloproteinases, elastases, and collagenases, that facilitate endothelial cells and tubule penetration through the extracellular matrix in cancer and arthritis progression [68–70]. The list of diseases that have angiogenesis as an underlying mechanism grows longer every year.

Although PAT generates high-resolution images of red blood cells in the microvasculature, [71–77] hemoglobin imaging cannot discriminate immature neovasculature from mature microvessels. Moreover, neovessel sprouting and bridging, which is a significant component of the neovascular contrast signal typically lacks any blood flow and is otherwise invisible to PA imaging. The $\alpha_v\beta_3$-integrin, a heterodimeric transmembrane glycoprotein,, is expressed by nonpolarized neovasculular endothelial cells [78] as well as numerous other cell types including macrophages [79], platelets [80], lymphocytes [81], smooth muscle cells [82] and tumor cells [83, 84]. Fortunately, the steric constraint of GNB and other particles exceeding 100nm diameter within the vasculature precludes significant interaction with nonendothelial integrin-expressing cells and greatly enhances neovascular target specificity [85].

To date, photoacoustic contrast agents targeting angiogenesis have been designed around integrin-targeted indocyanine green (ICG)-fluorescent-peptide conjugates [33, 86–90] and coupled to SWNT. Unfortunately small molecule agents easily diffuse from the neovascular vasculature and can bind the numerous cell types expressing $\alpha_v\beta_3$ integrin. SWNT, although interesting academically, pose challenges for clinical translation in terms of bioelimination and long term safety. $\alpha_v\beta_3$ GNB_1 was vascularly constrained and could not be detected microscopically beyond neovasculature of the Matrigel™ plug. This observation was further supported independently by other reports using copolymer and nanoemulsion particles. [85, 91]

$\alpha_v\beta_3$-targeted GNB_1 (160 nm), as opposed to GNB_S (90 nm) with a higher potential for extravasation or GNB_P (290 nm) which was expected to have a short circulatory half-life due to its overall mass and size. $\alpha_v\beta_3$-targeted GNB_1 was produced by microfluidization as discussed before by incorporating an $\alpha_v\beta_3$-peptidomimetic antagonist. $\alpha_v\beta_3$-peptidomimetic antagonist was conjugated to PEG_{2000}-phosphatidylethanolamine (0.1 mole%, Kereos, Inc, St. Louis, MO, USA). [92] This quinalone nonpeptide was developed by Lantheus Medical Imaging (Billerica, MA, US patent 6,511,648 and related patents) and produced by Kereos, Inc. The vitronectin antagonist was initially reported and characterized as the ^{111}In-DOTA conjugate RP478 and cyan 5.5 homologue TA145. [93] The specificity of the $\alpha_v\beta_3$-ligand mirrors that of the anti $\alpha_v\beta_3$-LM609 antibody [94] (Chemicon International, Inc., Temecula, CA) as assessed by staining and flow cytometry. The IC_{50} for $\alpha_v\beta_5$, $\alpha_5\beta_1$, and GP IIbIIIa was determined to be >10 μM (Lantheus Medical Imaging, unpublished data).

Neovascular imaging was performed *in vivo* in a Matrigel™ plug model of angiogenesis. Matrigel™ (750 μl) enriched with fibroblast growth factor-2 (500 nm/mL; Sigma Aldrich, St. Louis, MO) and heparin (64 U/mL) was implanted subcutaneously along the flank of mice. PAT imaging was performed prior to treatment and serially imaged over 5 hours post-injection on days 16 and 17 post Matrigel™ implantation. (Figure 16) Animals were randomly distributed into four groups and received: 1) $\alpha_v\beta_3$-gold nanobeacons ($\alpha_v\beta_3$-GNB$_1$, n = 6) $\alpha_v\beta_3$-nanobeacons without gold ($\alpha_v\beta_3$-NB) followed by $\alpha_v\beta_3$-GNB$_1$ (competitive blockage, n = 2) non-targeted gold nanobeacons (NT-GNB$_1$, n = 3) or saline (n = 2).

For the first time, high spatial resolution noninvasive PAT imaging of angiogenesis was demonstrated using a 10 MHz ultrasound receiver which clearly revealed the formation of nascent neovessel tubules, sprouts and bridges much of which was still without blood flow. $\alpha_v\beta_3$-GNB$_1$ produced a 600% increase in signal in a Matrigel™ plug mouse model relative to the inherent hemoglobin contrast pretreatment. Competitive inhibition of $\alpha_v\beta_3$-GNB$_1$ with $\alpha_v\beta_3$-NB (no gold) blocked contrast enhancement to pretreatment levels. Similar images in the saline control animals showed no change in vascular anatomy over the same time course. Indeed these images illustrate the genesis of neovasculature in the Matrigel™ plug model. A similar effect was seen with saline treated animals. Nontargeted GNB passively accumulated in the tortuous neovascularity, but provided low (less than half) contrast enhancement of the targeted agent. PA signal changes in the Matrigel™ plug were monitored serially over 5 hours or more (Figure 7).

The Matrigel angiogenesis study was supported histologically using a FGF Matrigel subcutaneous explant from FVB/N-TgN(TIE2LacZ)182Sato mice following injection (IV) of αvβ3-targeted rhodamine labelled GNB-M nanoparticles. These transgenic mice carry a beta-galactosidase reporter gene under the control of the murine Tek (Tie2) promoter. LacZ is expressed specifically in vascular endothelial cells in embryonic and adult mice. Microscopy definitively established that rhodamine-labeled $\alpha_v\beta_3$-GNB$_1$ targeted specifically to immature neovasculature expressing PECAM$^+$ but not Tie-2$^-$ localized along the implant periphery, but not to other peripheral microvasculature expressing PECAM$^+$ and Tie-2$^+$. (Figure 17) This experiment demonstrated that $\alpha_v\beta_3$-GNB$_1$ PA imaging sensitively and specifically discriminated angiogenesis from the adjacent microvasculature.

3. Small molecule-based and other exogenous PA agents

3.1 NIR cyanine dyes for real-time sentinel lymph node imaging

As we discussed previously, identification of SLN is a critical component of breast cancer staging and management. [95–97] Another approach to this issue was taken by Pan *et. al*. [98] wwith the development of a sub 20 nm "soft" polymeric nanoparticle. (Figure 18) This new agent was designed for rapid intraoperative administration with real time PA imaging. The intraoperative approach helps to eliminate anatomic plane displacement, which can complicate detection between the preoperative images and the patient repositioning in the OR. Moreover, by establishing a rapid operative procedure, the surgeon can determine the most direct approach to the node for resection minimizing potential secondary complications of the axillary dissection. The obvious key to this procedure is rapid signal generation with adequate intraoperative persistence.

The synthesis used by Pan et al utilized a one pot rapid synthetic pathway in which polysterene-*b*-poly(acrylic acid) (PS_8-*b*-PAA_{400}, Mnx10^3, 0.8-*b*-33.0, polydispersity index: PDI = 1.18, 0.00033 mmol, 0.5 mole%) was mixed with a co-surfactant, sorbitan monoleate, to restrict the particle diameter to 20 nm. A near infrared cyanine dye (ADS832WS, λ_{ex} = 824 nm, 1.90×10^5 L mol^{-1} cm^{-1}) was incorporated to act as a surrogate photoacoustic payload in this proof of concept study as shown in Figure 18.

Particle characterization was performed through many analytic techniques including TEM, AFM and DLS, which revealed the hydrodynamic particle diameter (Da_v) to be 16 ± 2 nm with a polydispersity of 0.021. The anhydrous particle diameter was (D_{ah} = 12 ± 0.4 nm) based on TEM images and presented a height of 15 ± 0.4 nm based on AFM images. Due to the incorporation of the NIR dye, the particle had high fluorescence with confirmed absorbencies at 750–860 nm. Additionally, these particles were found to possess long shelf-life stability (~40 days at ambient temperatures). Loading efficiency of dye was approximately 97%. Figure 18. Interestingly, the new particle also possessed theranostic potential, incorporating fumagillin and providing a prolonged release with dissolution testing *in vitro*.

Photoacoustic tomographic imaging of the new agent as a marker for axillary lymph nodes was studied in rats. Intradermal injection of the nanoparticles showed that the PA signals via maximum intensity projection (MAP) (Figure 20) produced a contrast enhancement of ~510% almost immediately. The signal enhancement was retained for 30 minutes at the SLNs and within 110 minutes, was almost completely drained. Such results suggest that these nanoparticles were delayed in transit within the lymph nodes but maintained their structural integrity and migrated out of the lymph nodes into the circulation system, which was attributed to their miniature size.

3.2 Copper as a contrast agent in PA imaging of sentinel lymph nodes

In an interesting study, Pan *et. al* [99] has demonstrated how copper could be utilized as an exogenous PA contrast agents for the identification of SLNs. The synthesis followed a self-assembly of Cu-neodecanoate complexes with polysorbates (sorbitan mono-9-octadecenoate poly(oxy-1,2-ethanediyl)) which were encapsulated within a phospholipid outer layer. As synthesized nanoparticles were subsequently purified by exhaustive dialysis to remove unbound copper (Figure 21).

The copper-rich nanoparticles had a hydrodynamic diameter of 86 ± 0.6 nm (D_h) with low polydispersity of 0.21 ± 0.02. Negative electrophoretic potential of −12 ± 07 mV indicated a complete encapsulation of the copper-polysorbate core with the surfactant. Further characterization of these nanoparticles was performed using TEM, AFM, SEM, and energy-dispersive X-ray spectroscopy (EDX). (Figure 22)

Cu-particles exhibited a PA signal that was significantly stronger and greater (The PA signal amplitude obtained from NanoCuN was ~650 mV compared to that of ~140 mV from blood) at 680 nm. Also, NanoCuN particles exhibited a strong absorption in the NIR region compared to a weak one displayed by hemoglobin. *In vivo* studies were conducted in rats as previously described to image the sentinel lymph nodes via PA imaging. Figure 23 shows a baseline image of the rat before NanoCuN administration presented as a maximum intensity projection (MIP) (Figure 23b). An image immediately after NanoCuN injection into the paw was showed initial uptake by the SLN (Figure 23c) which continued to increase for 60 minutes (Figure 23d).

3.3 Porphysome nanovesicles for multimodal biophotonic contrast agents

Many attempts at creating nanoparticles with optically active inorganic molecules have been studied, [100–103] but despite their drug loading efficiency and questions regarding long-term safety, [104–107] they have not been translated into the clinic. Organic nanoparticles have been shown to have more biocompatibility. [107] Based on these premises, Lovell *et. al* [108] synthesized a supramolecular self-assembled porphysome using porphyrin-lipid conjugates. Polyethylene glycol (PEG)-lipids were included to enhance *in vivo* pharmacokinetic properties as shown in Figure 24. These particles were spherical about 100 nm in diameter as confirmed by TEM. With greater magnification, it was shown that the porphysome structure contained two layers of higher-density material separated by 2 nm gaps. The porphysome showed two distinct absorption peaks at 400 nm and 680 nm, confirming the properties regarding the NIR nature of the particle. By inserting metal ions into the structure, Lovell was able to demonstrate the shifts in optical density bands at 440 nm and 670 nm, which also suggested that these porphysomes retained availability for metal chelation.

Porphysomes were tested for its photochemical properties by exposing them to laser irradiation. Thermal energy was released, which was similar in efficacy to that of gold nanorods. Photoacoustic amplitudes were atleast six fold (670 nm) higher for porphysomes than methylene blue, which is often used in the clinic for SLN detection, as mentioned earlier. The addition of detergent to the porphysome decreased the photoacoustic signal by six-fold while it had no effect on the methylene blue, indicating the necessary self-quenching nature of the porphysome to give off its PA signals (Figure 25a, b, c).

To further show that porphysomes could be used concurrently with photoacoustic tomography, *in vivo* studies were implemented by injecting porphysomes intradermally in rats. Figure 25d shows that the local lymphatic network was clearly visible and detectable within 15 minutes post-injection. Porphysomes displayed very strong photoacoustic signals affording distinct localization of the lymph node distinct from surroundings vessels. After 2 days, porphysomes accumulated within the tumor area and exhibited high fluorescence emission due to receptor-mediated endocytosis or more likely splenic uptake by macrophages which migrated to the inflammatory sites associated with the tumors, as is common for many particles.

4. Conclusion and future of photoacoustic tomography

For most of the preclinical work, the instrumentation is now commercially available; where as the majority of the work reported was conducted with laboratory-built robotic scanners. Visual Sonics, Inc., a subsidiary of SonoSite, Inc. was the first company to commercialize photoacoustics systems. They integrated photoacoustic capability into their existing Vevo LAZR™ platform to enhance high-resolution ultrasound-derived images with the sensitivity of optical imaging. This system provides real-time, in vivo imaging of deep tissue within a pebetration capability up to 1 cm. The integrated, 20Hz tunable laser can be operated within 680–970 nm and a resolution down to 45 μm caould be achieved. High optical contrast is co-registered with high-resolution imaging and an advanced analysis software package provided the ability to capture 2D and 3D images. Recently Endra Life Sciences launched Nexus128, a preclinical small animal imaging scanner with multimodal capabilities of photoacoustic imaging and computed tomography (CT). This system is the only commercially available fully 3-D photoacoustic CT scanner. The system is capable of generating fast, non-invasive quantification of physiological parameters such as tumor vasculature without ionizing radiation. Using Endra's Nexus 128™, Dominique Van de Sompel et al. demonstrated improving image quality by correcting temperature changes during long scans in both phantom and tissue samples. [109] Seno Medical Instruments, Inc. developed an Opto-acoustic system, which allows for the identification of tumors ~ 2 mm and has demonstrated the ability to see submillimeter structures. Recently, Seno Medical has licensed their technology to VisualSonics. TomoWave Loboratories, Inc., a Texas based company is also working towards the commercialization of this technique. As described in TomoWave website, their optoacoustic system LOUIS-3D™ consists of a Q-switched laser Spectra-Wave, generating wavelength 1064 nm, 532 nm and tunable in the near-infrared from 730 nm to 850 nm. Of note, the first PA scanners have been placed in clinics as prototypes for augmenting ultrasound techniques, such as SLN dye injection guidance.

As discussed above, photoacoustics imaging has been demonstrated by several groups using agents, e.g. organic dyes [110], gold nanoparticles [53–56], copper neodecanoate nanoparticles [99], single-walled carbon nanotubes (SWNT) [40, 52] and others [98]. These agents have shown definite potential for PA SLN mapping, imaging angiogenesis and melanoma with a depth capability of several centimeter, satisfactory spatial resolution. However, their use is not always out of questions. Organic dyes are extensively used in clinics but they are rather small (<2 nm), and thus can easily be transported into the echelon lymph nodes, causing a high possibility of producing false positives [111]. Often times they cause skin staining that leads to irritation. Gold nanoparticles of different sizes and morphologies are utilized widely, however, their optical properties are highly dependent on expensive and complicated surface chemistries. Their clinical use is also discouraged by the unpredictable high cost. Copper-based approach could potentially provide an innovative, inexpensive, and commercially viable approach. Although these particles were synthesized in a highly stable manner, copper is known to pose neurotoxicity [112]. SWNTs are inexpensive but the safety of these materials is still an ongoing debate [113]. With the constant advancement of PA technology, the future of this novel modality will also be dictated by the evolution of safer and sensitive molecularly targeted contrast agents.

The clinical opportunities garnered from the usage of PAT with approved dyes such as methylene blue are significant, and may be further improved with some of the preclinical agents discussed which would afford more robust and effective PA imaging. Moreover, the addition of physiological and targeted molecular imaging with PA alone and in concert with the new preclinical agents offers a significant expansion of the diagnostic utility of ultrasound, which remains one of the most cost effective and protable imaging modalities in medicine today.

References

1. Wang XD, Pang YJ, Ku G, Xie XY, Stoica G, Wang LHV. Noninvasive laserinduced photoacoustic tomography for structural and functional in vivo imaging of the brain. Nat. Biotechnol. 2003; 21:803–806. [PubMed: 12808463]
2. Li ML, Oh JT, Xie XY, Ku G, Wang W, Li C, Lungu G, Stoica G, Wang LHV. Simultaneous molecular and hypoxia imaging of brain tumors in vivo using spectroscopic photoacoustic tomography. Proc. of the IEEE. 2008; 96:481–489.
3. Wang XD, Xie XY, Ku G, Wang LHV. Noninvasive imaging of hemoglobin concentration and oxygenation in the rat brain using high-resolution photoacoustic tomography. J. Biomed. Opt. 2006; 11:024015. [PubMed: 16674205]
4. Lungu GF, Li ML, Xie XY, Wang LHV, Stoica G. In vivo imaging and characterization of hypoxia-induced neovascularization and tumor invasion. Int. J. Oncol. 2007; 30:45–54. [PubMed: 17143511]
5. Ku G, Wang XD, Stoica G, Wang LHV. Multiple-bandwidth photoacoustic tomography. Phys.Med. Biol. 2004; 49:1329–1338. [PubMed: 15128208]
6. Ku G, Wang XD, Xie XY, Stoica G, Wang LHV. Imaging of tumor angiogenesis in rat brains in vivo by photoacoustic tomography. Appl. Opt. 2005; 44:770–775. [PubMed: 15751858]
7. Schneider BP, Miller KD. Angiogenesis of breast cancer. J. Clin. Oncol. 2005; 23:1782–1790. [PubMed: 15755986]
8. Vaupel P, Mayer A, Briest S, Hockel M. Oxygen Transport to Tissue XXVI. 2005; 566:33–342.
9. Agarwal A, Huang SW, O’Donnell M, Day KC, Day M, Kotov N, Ashkenazi S. Targeted gold nano-rod contrast agent for prostate cancer detection by photoacoustic imaging. J. Appl. Phys. 2007; 102:064701–064704.
10. Zerda AD, Zavaleta C, Keren S, Vaithilingam S, Bodapati S, Liu Z, Levi J, Smith BR, Ma OT-J, Oralkan, Cheng Z, Chen X, Dai H, Khuri-Yakub BT, Gambhir SS. Carbon nanotubes as photoacoustic molecular imaging agents in living mice. Nat. Nanotech. 2008; 3:557–562.
11. Kojima H. Development of near infrared fluorescent probes for near infrared imaging. Yakugaku Zasshi. 2008; 128:1653. [PubMed: 18981701]
12. Ntziachristos V, Bremer C, Weissleder R. Fluorescence imaging with nearinfrared light: new technological advances that enable in vivo molecular imaging. Eur. Radiol. 2003; 13:195. [PubMed: 12541130]
13. Rostro-Kohanloo BC, Bickford LR, Payne CM, Day ES, Anderson LJ, Zhong M, Lee S, Mayer KM, Zal T, Adam L, Dinney CP, Drezek RA, West JL, Hafner JL. The stabilization and targeting of surfactant-synthesized gold nanorods. Nanotechnology. 2009; 20:434005. [PubMed: 19801751]
14. Pan D, Pramanik M, Senpan A, Yang X, Scott MJ, Song KH, Gaffney PJ, Wickline SA, Wang LV, Lanza GM. Molecular Photo Acoustic Imaging (PAI) with Ligand-Directed Gold Nanobeacons. Angew Chem. Int Ed. 2009; 48:4170–4173.
15. Skrabalak SE, Chen J, Au L, Lu X, Li X, Xia Y. Gold nanocages for biomedical applications. Adv Mater. 2007; 19:3177–3184. [PubMed: 18648528]
16. Skrabalak SE, Chen J, Sun Y, Lu X, Au L, Cobley C, Xia Y. Gold nanocages: synthesis, properties, and applications. Acc Chem Res. 2008; 41:1587–1595. [PubMed: 18570442]
17. Chen J, Yang M, Zhang Q, Cho EC, Cobley CM, Claus C, Kim C, Wang LV, Welch MJ, Xia Y. Gold nanocages: a novel class of multifunctional nanomaterials for theranostic applications. Adv Funct Mater. 2010; 20:3684–3694.
18. Hoelen CGA, de Mul FFM, Pongers R, Dekker A. Three-dimensional photoacoustic imaging of blood vessels in tissue. Opt Lett. 1998; 23:648–650. [PubMed: 18084605]
19. Kruger RA, Reinecke DR, Kruger GA. Thermoacoustic computed tomography-technical considerations. Med Phys. 1999; 26:1832–1837. [PubMed: 10505871]
20. Xu M, Wang LV. Photoacoustic imaging in biomedicine. Rev Sci Instrum. 2006; 77:1–22.
21. Wang Y, Xie X, Wang X, Ku G, Gill KL, O’Neal DP, Stoica G, Wang LV. Photoacoustic tomography of a nanoshell contrast agent in the in vivo rat brain. Nano Lett. 2004; 4:1689–1692.

22. Yang X, Skrabalak S, Li Z, Xia Y, Wang L. Photoacoustic tomography of a rat cerebral cortex in vivo with Au nanocages as an optical contrast agent. Nano Lett. 2007; 7:3798–3802. [PubMed: 18020475]

23. Morton DL, Wen DR, Wong JH, Economou JS, Cagle LA, Storm FK, Foshag LJ, Cochran AJ. Intraoperative lymphatic mapping and selective lymphadenectomy: technical details of a new procedure for clinical stage I melanoma. Arch Surg. 1992; 127:392–399. [PubMed: 1558490]

24. Krag DN, Weaver DL, Alex JC, Fairbank JT. Surgical resection and radiolocalization of the sentinel lymph node in breast cancer using a gamma probe. Surg Oncol. 1993; 2:335–340. [PubMed: 8130940]

25. Koyama Y, Talanov VS, Bernardo M, Hama Y, Regino CA, Brechbiel MW, Choyke PL, Kobayashi H. A dendrimer-based nanosized contrast agent dual-labeled for magnetic resonance and optical fluorescence imaging to localize the sentinel lymph node in mice. J Magn Reson Imag. 2007; 25:866–871.

26. Nakajima M, Takeda M, Kobayashi M, Suzuki S, Ohuchi N. Nano-sized fluorescent particles as new tracers for sentinel node detection: experimental model for decision of appropriate size and wavelength. Cancer Sci. 2005; 96:353–356. [PubMed: 15958058]

27. Michel SC, Keller TM, Frohlich JM, Fink D, Caduff R, Seifert B, Marincek B, Kubik-Huch RA. Preoperative breast cancer staging: MR imaging of the axilla with Ultrasmall superparamagnetic iron oxide enhancement. Radiology. 2002; 225:527–536. [PubMed: 12409591]

28. Torchia MG, Nason R, Danzinger R, Lewis JM, Thliveris JA. Interstitial MR lymphangiography for the detection of sentinel lymph nodes. J Surg Oncol. 2001; 78:151–156. [PubMed: 11745796]

29. Krag DN, Anderson SJ, Julian TB, Brown AM, Harlow SP, Costantino JP, Ashikaga T, Weaver DL, Mamounas, Jalovec LM, Frazier TG, Noyes RD, Robidoux A, Scarth HMC, Wolmark N. Sentinellymph-node resection compared with conventional axillary-lymph-node dissection in clinically node-negative patients with breast cancer: overall survival findings from the NSABP B-32 randomised phase 3 trial. Lancet Oncol. 2010; 11:927–933. [PubMed: 20863759]

30. Song KH, Kim C, Cobley CM, Xia Y, Wang LV. Near-infrared gold nanocages as a new class of tracers for photoacoustic sentinel lymph node mapping on a rat model. Nano Lett. 2009; 9:183–188. [PubMed: 19072058]

31. Kim C, Cho EC, Chen J, Song KH, Au L, Favazza C, Zhang Q, Cobley CM, Gao F, Xia Y, Wang LV. In vivo molecular photoacoustic tomography of melanomas targeted by bioconjugated gold nanocages. ACS Nano. 2010; 4:4559–4564. [PubMed: 20731439]

32. Zharov VP, Galanzha EI, Shashkov EV, Kim J-W, Khlebtsov NG, Tuchin VV. Photoacoustic flow cytometry: principle and application for real-time detection of circulating single nanoparticles, pathogens, and contrast dyes in vivo. J Biomed Opt. 2007; 12:051503. [PubMed: 17994867]

33. de la Zerda A, Zavaleta C, Keren S, Vaithilingam S, Bodapati S, Liu Z, Levi J, Smith BR, Ma TJ, Oralkan O, Cheng Z, Chen X, Dai H, Khuri-Yakub BT, Gambhir SS. Carbon nanotubes as photoacoustic molecular imaging agents in living mice. Nat Nanotechnol. 2008; 3:557–562. [PubMed: 18772918]

34. de la Zerda A, Liu Z, Bodapati S, Teed R, Vaithilingam S, Khuri-Yakub BT, Chen X, Dai H, Gambhir SS. Ultrahigh sensitivity carbon nanotube agents for photoacoustic molecular imaging in living mice. Nano Lett. 2010; 10:2168–2172. [PubMed: 20499887]

35. Galanzha EI, Shashkov EV, Kelly T, Kim J-W, Yang L, Zharov VP. In vivo magnetic enrichment and multiplex photoacoustic detection of circulating tumour cells. Nat Nanotechnol. 2009; 4:855–860. [PubMed: 19915570]

36. Kim J-W, Galanzha EI, Shashkov EV, Moon H-M, Zharov VP. Golden carbon nanotubes as multimodal photoacoustic and photothermal high-contrast molecular agents. Nat Nanotechnol. 2009; 4:688–694. [PubMed: 19809462]

37. Galanzha EI, Shashkov EV, Kokoshka MS, Myhill JA, Zharov. In vivo noninvasive detection of metastatic cells in vasculature and sentinel lymph nodes by photoacoustic cytomery. Laser Surg Med. 2008; S20:81–82.

38. Galanzha EI, Kokoska MS, Shashkov EV, Kim J-W, Tuchin VV, Zharov VP. In vivo fiber-based multicolor photoacoustic detection and photothermal purging of metastasis in sentinel lymph nodes targeted by nanoparticles. J Biophotonics. 2009; 2:528–539. [PubMed: 19743443]

39. Pramanik M, Song KH, Swierczewska M, Green D, Sitharaman B, Wang LV. In vivo carbon nanotube-enhanced non-invasive photoacoustic mapping of the sentinel lymph node. Phys Med Biol. 2009; 54:3291–3301. [PubMed: 19430111]

40. Pramanik M, Swierczewska M, Green D, Sitharaman B, Wang LV. Single-walled carbon nanotubes as a multimodal-thermoacoustic and photoacoustic-contrast agent. J Biomed Opt. 2009; 14:034018. [PubMed: 19566311]

41. Galanzha EI, Kim J-W, Zharov VP. Integrated nanotechnology based photoacoustic and photothermal flow cytometry platform for in vivo detection and killing of circulating cancer stem cells. J Biophoton. 2009; 2:725–735.

42. Zharov VP, Galitovsky V, Viegas M. Photothermal detection of local thermal effects during selective nanophotothermolysis. Appl Phys Lett. 2003; 83:4897–4899.

43. Zharov VP, Galitovskaya EN, Jonson C, Kelly T. Synergistic enhancement of selective nanophotothermolysis with gold nanoclusters: potential for cancer therapy. Laser Surg Med. 2005; 37:219–226.

44. Zharov VP, Letfullin RR, Galitovskaya EN. Microbubbles-overlapping mode for laser killing of cancer cells with absorbing nanoparticle clusters. J Phys D Appl Phys. 2005; 38:2571–258.

45. Zharov VP, Kim J-W, Everts M, Curiel DT. Self-assembling nanoclusters in living system application for integrated photothermal nanodiagnostics and nanotherapy. Nanomedicine. 2005; 1:326–345. [PubMed: 17292107]

46. Zharov VP, Mercer KE, Galitovskaya EN, Smeltzer MS. Photothermal nanotherapeutics and nanodiagnostics for selective killing of bacteria targeted with gold nanoparticles. Biophys J. 2006; 90:619–628. [PubMed: 16239330]

47. Kim J-W, Galanzha EI, Shashkov EV, Kotagiri N, Zharov VP. Photothermal antimicrobial nanotherapy and nanodiagnostics with self-assembling carbon nanotube clusters. Lasers Surg Med. 2007; 39:622–634. [PubMed: 17868103]

48. Khlebtsov B, Zharov V, Melnikov A, Tuchin V, Khlebtsov N. Optical amplification of photothermal therapy with gold nanoparticles and nanoclusters. Nanotechnology. 2006; 17:5167–5179.

49. Hirsch LR, Stafford RJ, Bankson JA, Sershen SR, Rivera B, Price RE, Hazle JD, Halas NJ, West JL. Nanoshell-mediated thermal therapy of tumors under magnetic resonance guidance. Proc Natl Acad Sci USA. 2003; 100:13549–13554. [PubMed: 14597719]

50. Kam NW, O'Connell M, Wisdom JA, Dai H. Carbon nanotubes as multifunctional biological transporters and near-infrared agents for selective cancer cell destruction. Proc Natl Acad Sci USA. 2005; 102:11600–11605. [PubMed: 16087878]

51. Liu Z, Sun X, Nakayama-Ratchford N, Dai H. Chemistry on watersoluble carbon nanotubes for drug loading and delivery. ACS Nano. 2007; 1:50–56. [PubMed: 19203129]

52. Liu Z, Cai W, He L, Nakayama N, Chen K, Sun X, Chen X, Dai H. In vivo biodistribution and highly efficient tumour targeting of carbon nanotubes in mice. Nat Nanotechnol. 2007; 2:47–52. [PubMed: 18654207]

53. Pan D, Pramanik M, Zhang H, Senpan A, Schmieder A, Wickline SA, Wang LV, Lanza GM. Photoacoustics tomography differentiates early vulnerable neoangiogenesis from mature vasculature in vivo. JACC. 2011; 57:E1595.

54. Pan D, Pramanik M, Senpan A, Ghosh S, Wickline SA, Wang LV, Lanza GM. Near infrared photoacoustic detection of sentinel lymphnodes with gold nanobeacons. Biomaterials. 2010; 31:4088–4093. [PubMed: 20172607]

55. Pan D, Pramanik M, Senpan A, Wickline SA, Wang LV, Lanza GM. A facile synthesis of novel self-assembled gold nanorods designed for near-infrared imaging. J. Nanosci. Nanotech. 2010; 10:8118–8123.

56. Pan D, Pramanik M, Senpan A, Stacy A, Zhang H, Wickline SA, Wang LV, Lanza GM. Molecular photoacoustic imaging of angiogenesis with integrin targeted gold nanobeacons. Faseb J. 2011; 25:378–388.

57. Raut S, Gaffney PJ. Evaluation of the fibrin binding profile of two anti-fibrin monoclonal antibodies. Throm. Haemostasos. 1996; 76:56–64.

58. Gamelin J, Aguirre A, Maurudis A, Huang F, Castillo D, Wang LV, Zhu Q. Curved array photoacoustic tomographic system for small animal imaging. J Biomed Opt. 2008; 13(2):024007. [PubMed: 18465970]
59. Pramanik M, Ku G, Li CH, Wang LHV. Design and evaluation of a novel breast cancer detection system combining both thermoacoustic (TA) and photoacoustic (PA) tomography. Med. Phys. 2008; 35:2218–2223. [PubMed: 18649451]
60. Krag D, Weaver D, Ashikaga T, Moffat F, Klimberg VS, Shriver C, Feldman S, Kusminsky R, Gadd M, Kuhn J, Harlow S, Beitsch P. The sentinel node in breast cancer – a multicenter validation study. N Engl J Med. 1998; 339:941–946. [PubMed: 9753708]
61. McMasters KM, Tuttle TM, Carlson DJ, Brown CM, Noyes RD, Glaser RL, Vennekotter DJ, Turk PS, Tate PS, Sardi A, Cerrito PB, Edwards MJ. Sentinel lymph node biopsy for breast cancer: a suitable alternative to routine axillary dissection in multi-institutional practice when optimal technique is used. J Clin Oncol. 2000; 18:2560–2566. [PubMed: 10893287]
62. Chen SL, Iddings DM, Scheri RP, Bilchik AJ. Lymphatic Mapping and Sentinel Node Analysis. CA Cancer J Clin. 2006; 56:292–309. [PubMed: 17005598]
63. Laruelle G, Francios J, Billon L. Self-assembly in aqueous media of amphiphilic poly acrylic acid based di-block copolymers synthesized by direct nitroxidemediated polymerization. Macromol Rapid Commun. 2004; 25:1839–1844.
64. Huang HY, Kowalewski T, Remsen EE, Gertzmann R, Wooley KL. Hydrogelcoated glassy nanospheres: A novel method for the synthesis of shell crosslinked knedels. J Am Chem Soc. 1997; 119:11653–11659.
65. Wu J, Eisenberg A. Proton diffusion across membranes of vesicles of poly(styrene-b-acrylic acid) diblock copolymers. J Am Chem Soc. 2006; 128:2880–2884. [PubMed: 16506766]
66. Xu J, Sun G, Rossin R, Hagooly A, Li Z, Fukukawa K, Messmore BW, Moore DA, Welch MJ, Hawker CJ, Wooley KL. Labeling of Polymer Nanostructures for Medical Imaging: Importance of charge density, spacer length, and crosslinking extents. Macromolecules. 2007; 40:2971–2973. [PubMed: 18779874]
67. Zhang HF, Maslov K, Stoica G, Wang LHV. Functional photoacoustic microscopy for high-resolution and noninvasive in vivo imaging. Nat. Biotechnol. 2006; 24:848–851. [PubMed: 16823374]
68. Brooks PC, Clark RAF, Cheresh DA. Requirement of vascular integrin avb3 for angiogenesis. Science. 1994; 264:569–571. [PubMed: 7512751]
69. Winter P, Neubauer A, Caruthers S, Harris T, Robertson J, Williams T, Schmieder A, Hu G, Allen J, Lacy E, Wickline S, Lanza G. Endothelial alpha(nu)beta(3)-integrin targeted fumagillin nanoparticles inhibit angiogenesis in atherosclerosis. Arterioscler. Thromb. Vasc. Biol. 2006; 26:2103–2109. [PubMed: 16825592]
70. Winter PM, Schmieder AH, Caruthers SD, Keene JL, Zhang H, Wickline SA, Lanza GM. Minute dosages of alpha(nu)beta3-targeted fumagillin nanoparticles impair Vx-2 tumor angiogenesis and development in rabbits. FASEB J. 2008; 22:2758–2767. [PubMed: 18362202]
71. Wang XD, Pang YJ, Ku G, Xie XY, Stoica G, Wang LV. Noninvasive laserinduced photoacoustic tomography for structural and functional in vivo imaging of the brain. Nat. Biotech. 2003; 21:803–806.
72. Siphanto RI, Thumma KK, Kolkman RG, van Leeuwen TG, de Mul FF, van Neck JW, van Adrichem LN, Steenbergen W. Serial noninvasive photoacoustic imaging of neovascularization in tumor angiogenesis. Opt. Express. 2005; 13:89–95. [PubMed: 19488331]
73. Maslov K, Zhang HF, Hu S, Wang LV. Optical-resolution photoacoustic microscopy for in vivo imaging of single capillaries. Optics Lett. 2008; 33:929–931.
74. Lao Y, Xing D, Yang S, Xiang L. Noninvasive photoacoustic imaging of the developing vasculature during early tumor growth. Phys. Med. Biol. 2008; 53:4203–4212. [PubMed: 18635896]
75. Zhang EZ, Laufer JG, Pedley RB, Beard PC. In vivo high-resolution 3D photoacoustic imaging of superficial vascular anatomy. Phys. Med. Biol. 2009; 54:1035–1046. [PubMed: 19168938]
76. Jose J, Manohar S, Kolkman RG, Steenbergen W, van Leeuwen TG. Imaging of tumor vasculature using Twente photoacoustic systems. J. Biophotonics. 2009; 2:701–717. [PubMed: 19718681]

77. Hu S, Oladipupo S, Yao J, Santeford AC, Maslov K, Kovalski J, Arbeit JM, Wang LV. Opticalresolution photoacoustic microscopy of angiogenesis in a transgenic mouse model. Proc. SPIE. 2010; 7564:756406.
78. Cheresh DA. Integrins in thrombosis, wound healing and cancer. Biochem. Soc. Trans. 1991; 19:835–838. [PubMed: 1794568]
79. Friedlander M, Theesfeld CL, Sugita M, Fruttiger M, Thomas MA, Chang S, Cheresh DA. Involvement of integrins anb3 and anb5 in ocular neovascular diseases. Proc. Natl Acad. Sci. USA. 1996; 93:9764–9769. [PubMed: 8790405]
80. De Nichilo M, Burns G. Granulocytemacrophage and macrophage colonystimulating factors differentially regulate a v integrin expression on cultured human macrophages. Proc. Natl Acad. Sci. USA. 1993; 90:2517–2521. [PubMed: 7681600]
81. Helluin O, Chan C, Vilaire G, Mousa S, DeGrado WF, Bennett JS. The activation state of avb3 regulates platelet and lymphocyte adhesion to intact and thrombin-cleaved osteopontin. J. Biol. Chem. 2000; 275:18337–18343. [PubMed: 10751402]
82. Itoh H, Nelson P, Mureebe L, Horowitz A, Kent K. The role of integrins in saphenous vein vascular smooth muscle cell migration. J. Vasc. Surg. 1997; 25:1061–1069. [PubMed: 9201167]
83. Carreiras F, Denoux Y, Staedel C, Lehman M, Sichel F, Gauduchon P. Expression and localization of a v integrins and their ligand vitronectin in normal ovarian epithelium and in ovarian carcinoma. Gynecol. Oncol. 1996; 62:260–267. [PubMed: 8751559]
84. Kageshita T, Hamby CV, Hirai S, Kimura T, Ono T, Ferrone S. Differential clinical significance of a(v)B(3) expression in primary lesions of acral lentiginous melanoma and of other melanoma histotypes. Int. J. Cancer. 2000; 89:153–159. [PubMed: 10754493]
85. Hu G, Lijowski M, Zhang H, Partlow KC, Caruthers SD, Kiefer G, Gulyas G, Athey P, Scott MJ, Wickline SA, Lanza GM. Imaging of Vx-2 rabbit tumors with avb3-integrintargeted 111In nanoparticles. Int. J. Cancer. 2007; 120:1951–1957. [PubMed: 17278104]
86. Wang LV, Xie X, Oh JT, Li MN, Ku G, Ke S, Similache S, Li C, Stoica G. Combined photoacoustic and molecular fluorescence imaging in vivo. IEEE Eng. Med. Biol. Proc. 2005; 7:190–192.
87. Xie X, Oh JT, Li ML, Ku G, Wang X, Ke S, Li C, Similache S, Stoica G, Wang LV. Photoacoustic tomography and molecular fluorescence imaging: Dual modality imaging of small animal brains in vivo. Proc. SPIE. 2005; 5697:107–110.
88. Welsher K, Liu Z, Sherlock SP, Robinson JT, Chen Z, Daranciang D, Dai H. A route to brightly fluorescent carbon nanotubes for near-infrared imaging in mice Nat. Nanotechnol. 2009; 4:773–780.
89. Xie X, Li ML, Oh JT, Ku G, Wang W, Li C, Similache S, Lungu GF, Stoica G, Wang LV. Photoacoustic molecular imaging of small animals in vivo. Proc. SPIE. 2006; 6086:608606.
90. Xiang L, Yuan Y, Xing D, Ou Z, Yang S, Zhou F. Photoacoustic molecular imaging with antibody-functionalized single-walled carbon nanotubes for early diagnosis of tumor. J. Biomed. Opt. 2009; 14:021008. [PubMed: 19405721]
91. Weissleder R, Bogdanov A Jr, Tung CH, Weinmann HJ. Size optimization of synthetic graft copolymers for in vivo angiogenesis imaging. Bioconjug. Chem. 2001; 12:213–219. [PubMed: 11312682]
92. Harris, TD.; Rajopadhye, M. Vitronectin receptor antagonist pharmaceuticals. US patent. 6,511,648.
93. Meoli DF, Sadeghi MM, Krassilnikova S, Bourke BN, Giordano FJ, Dione DP, Su H, Edwards DS, Liu S, Harris TD, Madri JA, Zaret BL, Sinusas AJ. Noninvasive imaging of myocardial angiogenesis following experimental myocardial infarction. J Clin Invest. 2004; 113:1684–1691. [PubMed: 15199403]
94. Miyauchi A, Alvarez J, Greenfield EM, Teti A, Grano M, Colucci S, Zambonin-Zallone A, Ross FP, Teitelbaum SL, Cheresh D, et al. Recognition of osteopontin and related peptides by an alpha v beta 3 integrin stimulates immediate cell signals in osteoclasts. J Biol Chem. 1991; 266:20369–20374. [PubMed: 1939092]

95. Cady B, Stone MD, Schuler JG. The new era in breast cancer. Invasion, size, and nodal involvement dramatically decreasing as a result of mammographic screening Arch. Surg. 1996; 131:301–308.

96. Haffty BG, Ward B, Pathare P. Reappraisal of the role of axillary lymph node dissection in the conservative treatment of breast cancer. J. Clin. Oncol. 1997; 15:691–700. [PubMed: 9053495]

97. Veronesi U, Paganelli G, Viale G. A Randomized Comparison of Sentinel-Node Biopsy with Routine Axillary Dissection in Breast Cancer. N. Engl. J. Med. 2003; 349:546–553. [PubMed: 12904519]

98. Pan D, Cai X, Kim B, Stacy AL, Wang LV, Lanza GM. Rapid Synthesis of Near Infrared Polymeric Micelles for Real-Time Sentinel Lymph Node Imaging. Adv. Healthcare Mater. 2012; 1:582–589.

99. Pan D, Cai X, Yalaz C, Senpan A, Omanakuttan K, Wickline SA, Wang LV, Lanza GM. Photoacoustic Sentinel Lymph Node Imaging with Self-Assembled Copper Neodecanoate Nanoparticles. ACS Nano. 2012; 6:1260–1267. [PubMed: 22229462]

100. Chan WC, Nie S. Quantum dot bioconjugates for ultrasensitive nonisotopic detection. Science. 1998; 281:2016–2018. [PubMed: 9748158]

101. Storhoff JJ, Lucas AD, Garimella V, Bao YP, Muller UR. Homogeneous detection of unamplified genomic DNA sequences based on colorimetric scatter of gold nanoparticle probes. Nature Biotechnol. 2004; 22:883–887. [PubMed: 15170215]

102. Oraevsky AA. Laser optoacoustic tomography for medical diagnostics: Principles. Pro. SPIE. 1996; 2676:22–31.

103. Lal S, Clare SE, Halas NJ. Nanoshell-enabled photothermal cancer thereapy: Impending clinical impact. Acc. Chem. Res. 2008; 41:1842–1851. [PubMed: 19053240]

104. Ghosh P, Han G, De M, Kim CK, Rotello VM. Gold nanoparticles in delivery applications. Adv. Drug. Deliv. Rev. 2008; 60:1307–1315. [PubMed: 18555555]

105. Lewinski N, Colvin V, Drezek R. Cytotoxicity of nanoparticles. Small. 2008; 4:26–49. [PubMed: 18165959]

106. Nel A, Xia T, Madler L, Li N. Toxic potential of materials at the nanolevel. Science. 2006; 311:622–627. [PubMed: 16456071]

107. Peer D, Karp JM, Hong S, Farokhzad OC, Margalit R, Langer R. Nanocarriers as an emerging platform for cancer therapy. Nature Nanotech. 2007; 2:751–760.

108. Lovell JF, Jin CS, Huynh E, Jin H, Kim C, Rubinstein JL, Chan WC, Cao W, Wang LV, Zheng G. Porphysome nanovesicles generated by porphyrin bilayers for use as multimodal biophotonic contrast agents. Nature Materials. 2011; 10:324–332.

109. Van de Sompel D, Sasportas LS, Dragulescu-Andrasi A, Bohndiek S, Gambhir SS. Improving Image Quality by Accounting for Changes in Water Temperature during a Photoacoustic Tomography Scan. PLoS ONE. 2012; 7(10):e45337. [PubMed: 23071512]

110. Song KH, Stein EW, Margenthaler JA, Wang LV. Noninvasive photoacoustic identification of sentinel lymph nodes containing methylene blue in vivo in a rat model. J Biomed Opt. 2008; 13:054033. [PubMed: 19021413]

111. Sohrabnezhad S, Pourahmad A, Sadjadi MA. New methylene blue incorporated in mordenite zeolite as humidity sensor material. Mater. Lett. 2007; 61:2311–2314.

112. Brewer GJ. Copper toxicity in the general population. Clin. Neurophysiol. 2010; 121:459–460. [PubMed: 20071223]

113. Yang S-T, Luo J, Zhou Q, Wang H. Pharmacokinetics, Metabolism and Toxicity of Carbon Nanotubes for Biomedical Purposes. Theranostics. 2012; 2(3):271–282. [PubMed: 22509195]

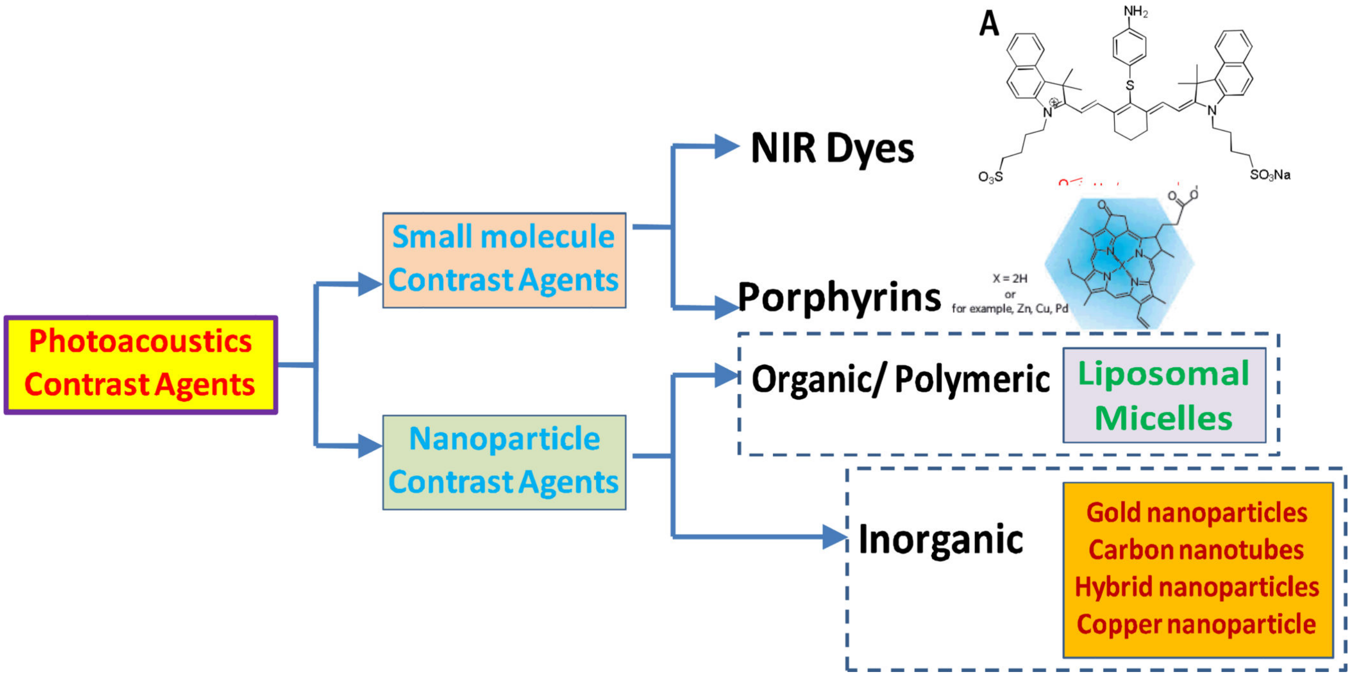

Figure 1.

Different classes of photoacoustic contrast agents.

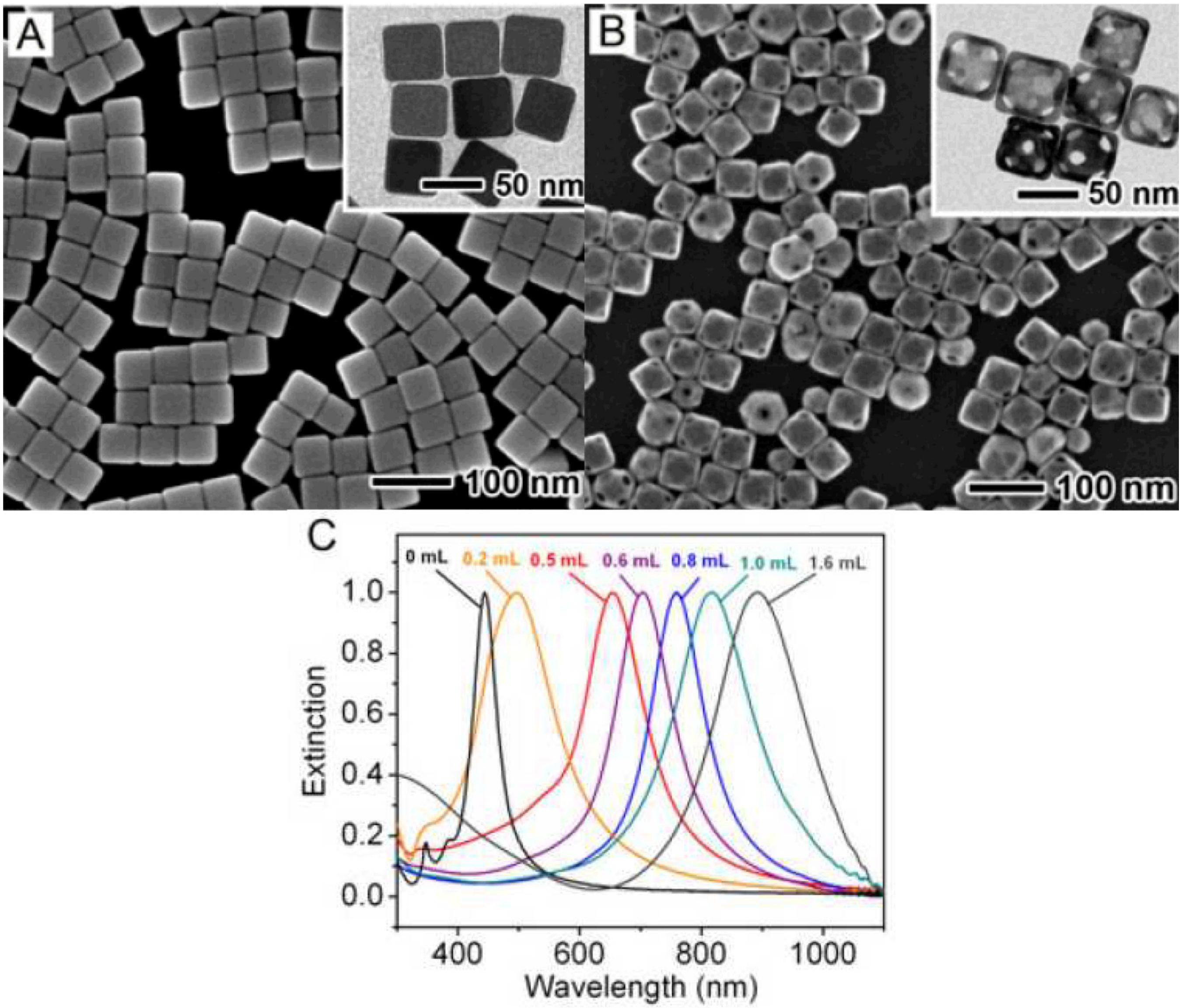

Figure 2.

SEM images of (A) Ag nanocubes and (B) AuNCs. The inset shows the corresponding TEM images of the same sample. (C) UV-vis spectra of the samples obtained by titrating Ag nanocubes with different volumes of 0.1 mM $HAuCl_4$ solution.

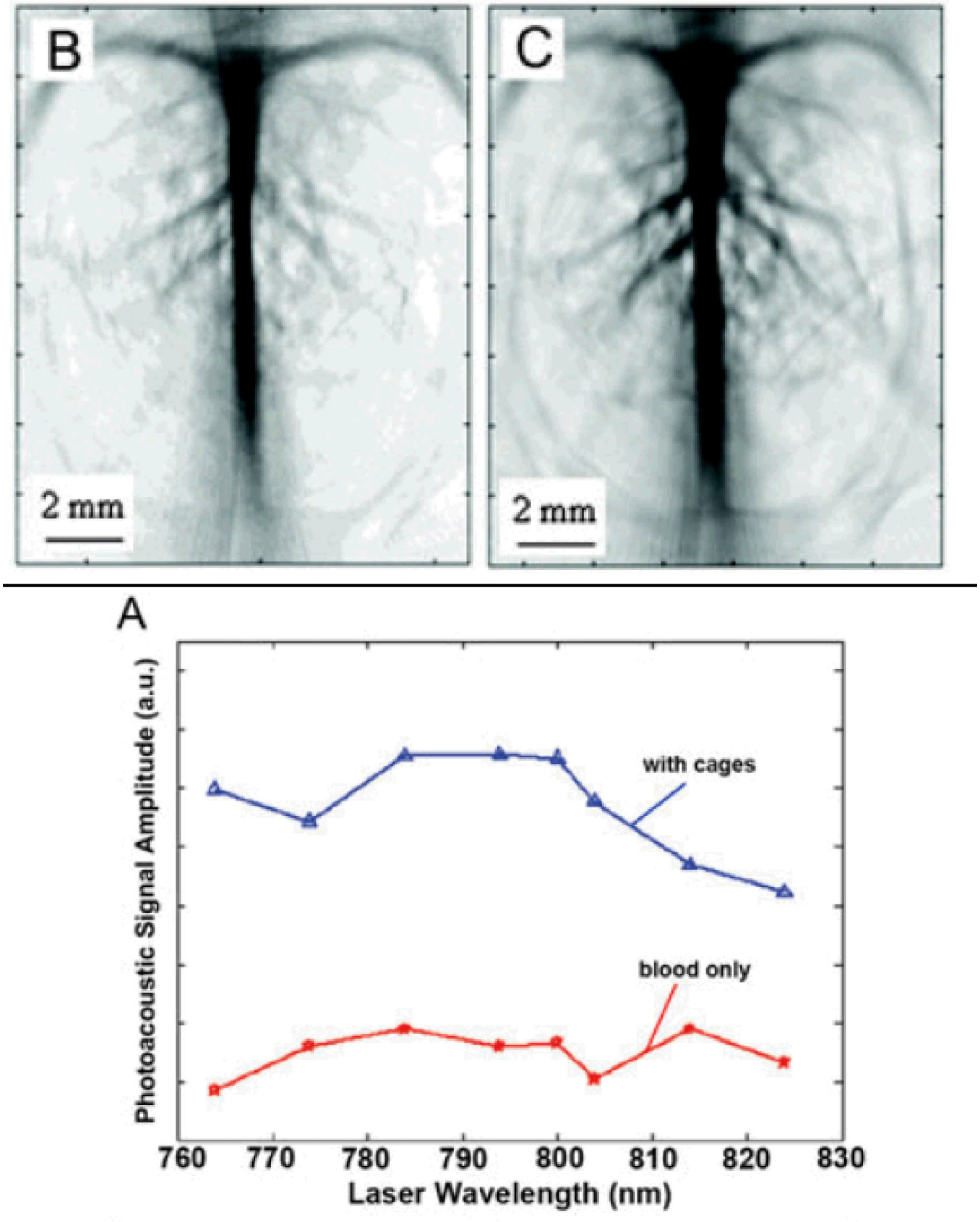

Figure 3.

(A) The measured PA signal amplitude generated with and without AuNCs in rat blood at several wavelengths. Noninvasive PA imaging of a rat's cerebral cortex, (B) before the injection of AuNCs and (C) about 2 h after the final injection of nanocages, which is the peak enhancement point. Reproduced with permission from (22), copyright 2007 American Chemical Society.

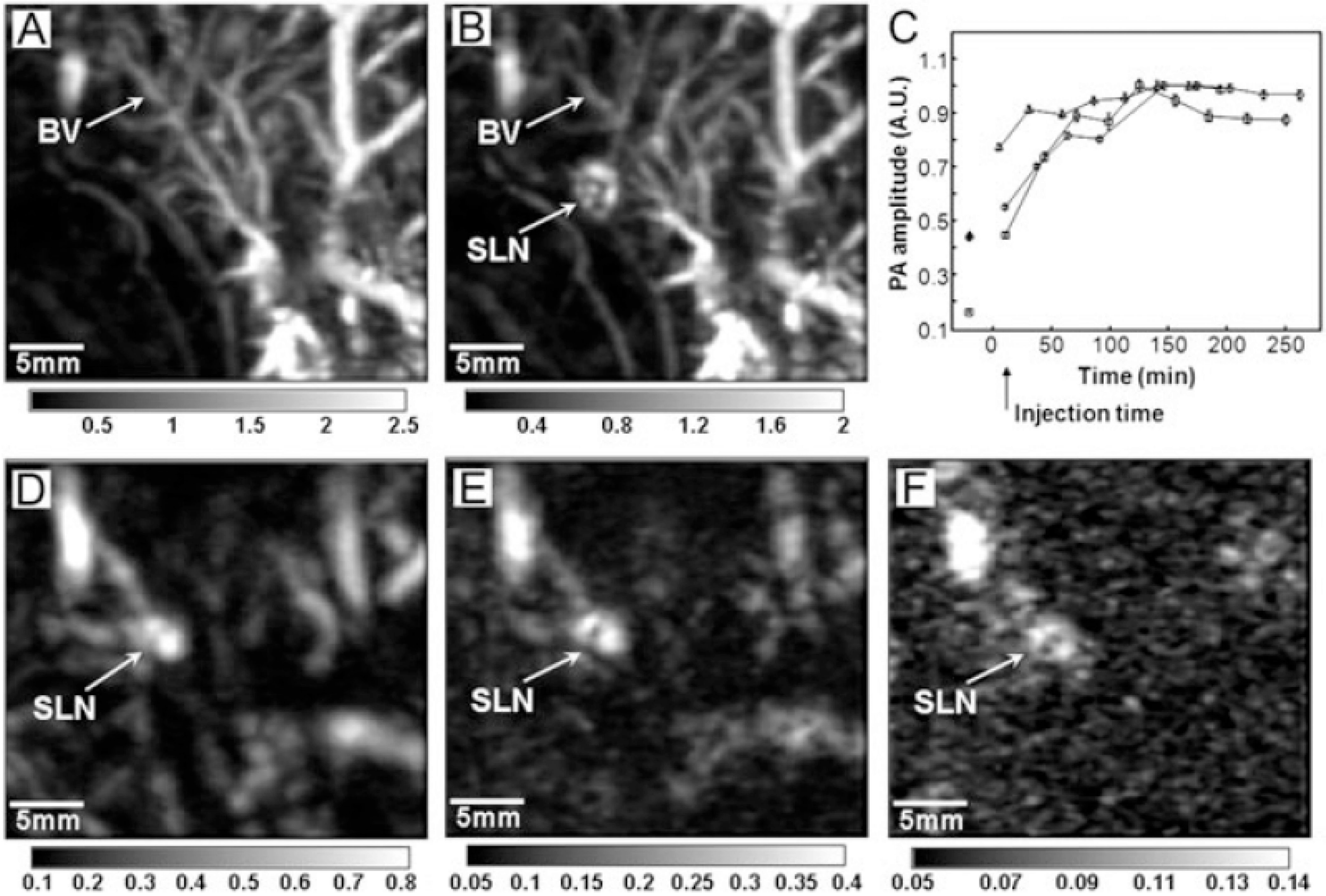

Figure 4.

PA images of the axillary region of a rat taken (A) before and (B) 28 min after the injection of AuNCs. (C) The changes of PA signal amplitude as a function of the post-injection time. After the injection, PA signals increased with time, which means gradual accumulations of the nanocages. (D–F) Depth capability of SLN mapping with AuNCs. The PA images were acquired after the injection of nanocages for: (D) 126 min with a total imaging depth of 10 mm by placing a layer of chicken breast tissue on the axillary region; (E) 165 min with a total imaging depth of 21 mm by adding another layer of chicken breast tissue; and (F) 226 min with a total imaging depth of 33 mm by using three layers of chicken breast tissue. The bars represent the optical absorption. BV, blood vessel. SLN, sentinel lymph node. Reproduced with permission from (30), copyright 2009 American Chemical Society.

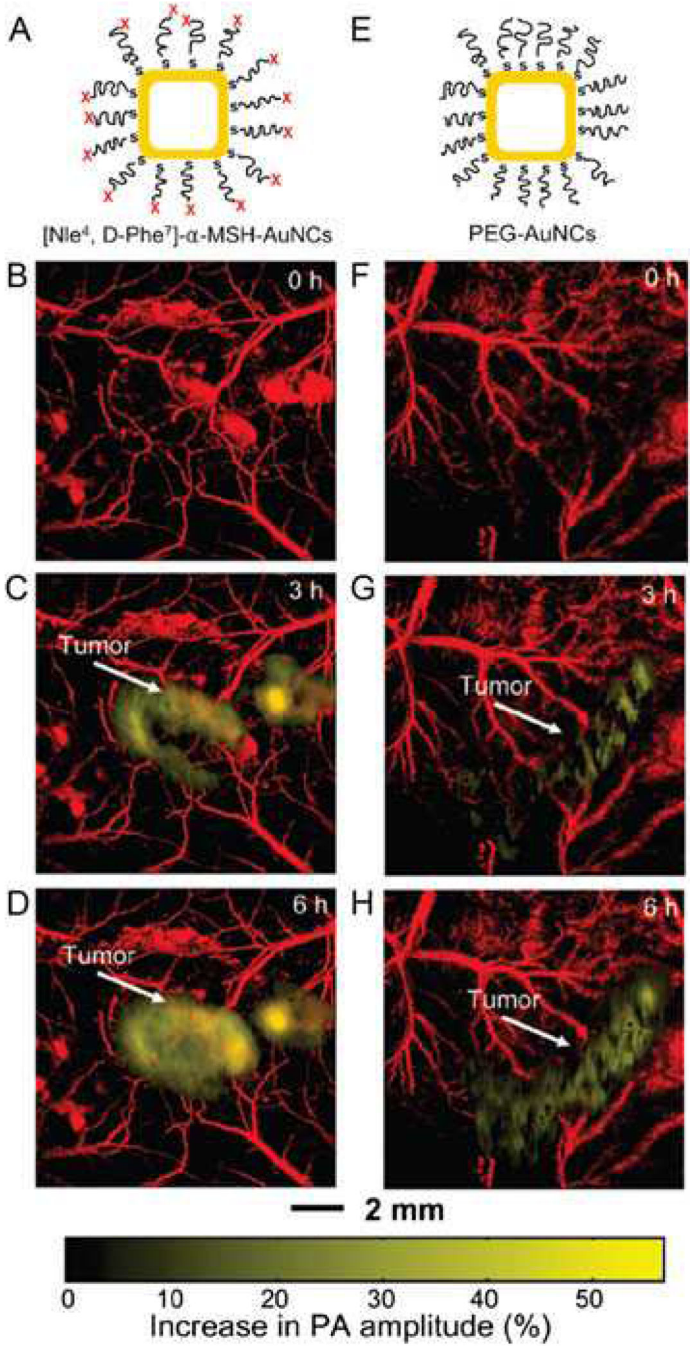

Figure 5.

In vivo noninvasive PA time-course coronal MAP images of B16 melanomas using [Nle^4, D-Phe^7]-a-MSH- and PEG-AuNCs. (A, E) a schematic of the [Nle^4, D-Phe^7]-a-MSH- and PEG-AuNCs. Time-course PA images of the B16 melanomas after intravenous injection with 100 μl of 10 nM (B–D) [Nle^4, D-Phe^7]-a-MSH- and (f–H) PEG-AuNCs through the tail vein. the background vasculature images were obtained using the PA microscope at 570 nm (ultrasonic frequency = 50 MHz), and the melanoma images were obtained using the PA macroscope at 778 nm (ultrasonic frequency = 10 MHz). reproduced with permission from (31), copyright 2010 American Chemical Society.

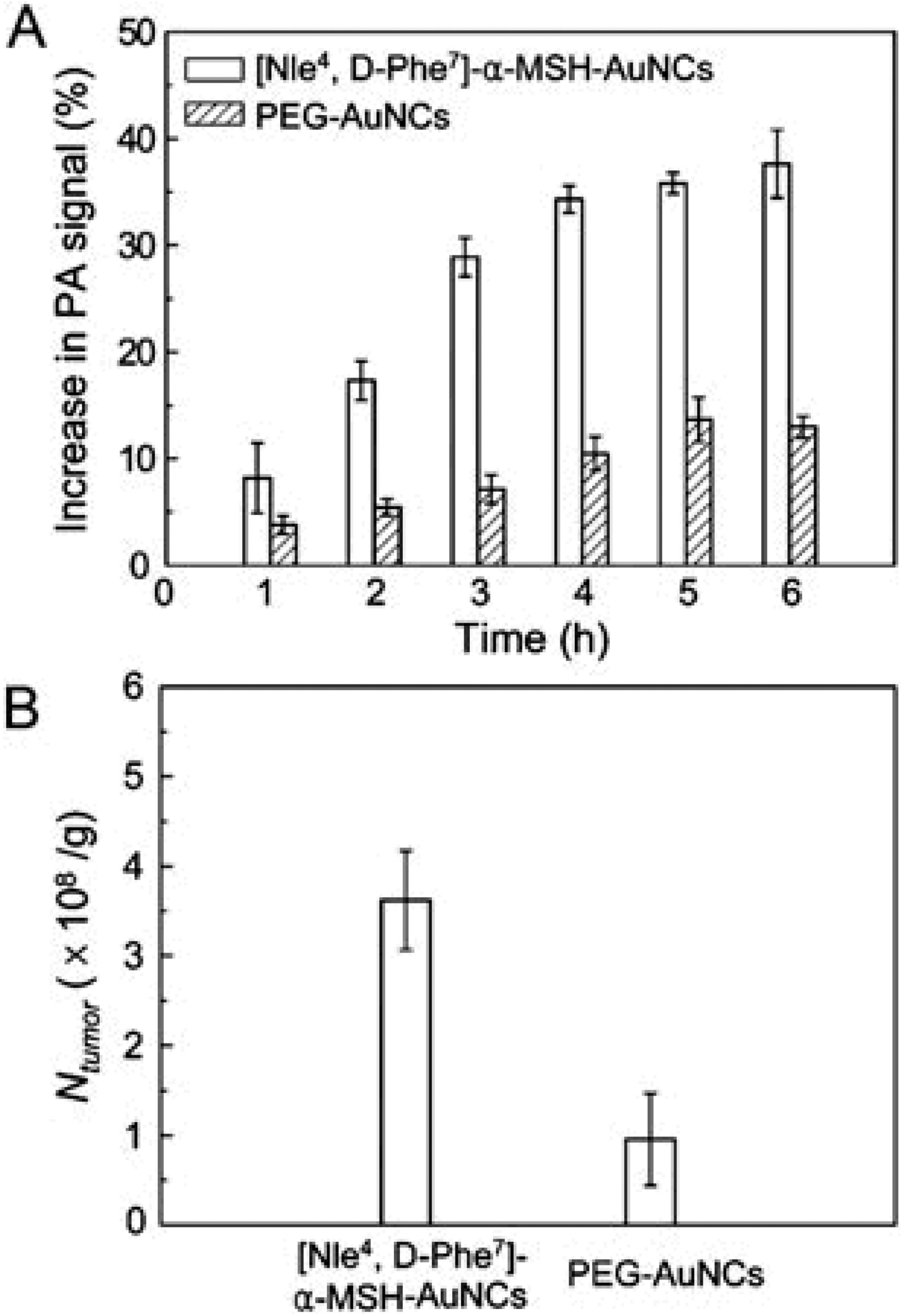

Figure 6.

(A) Increase of PA amplitude in the melanoma tumors after intravenous injection of [Nle^4, D-Phe^7]-a-MSH- and PEG-AuNCs (n=4 mice for each group), respectively, for different periods of time. The PA signals increased up to 38 ±6 % for [Nle^4, D-Phe^7]-a-MSH-AuNCs while the maximum signal increase only reached 13 ± 2% for PEG-AuNCs at a post-injection time of 6 h ($p < 0.0001$). (B) The average number of AuNCs accumulated in the melanomas dissected at 6 h post injection for the two types of AuNCs as measured by ICP-

MS. Here N_{tumor} denotes the number of AuNCs per unit tumor mass (g). Reproduced with permission from (31), copyright 2010 American Chemical Society.

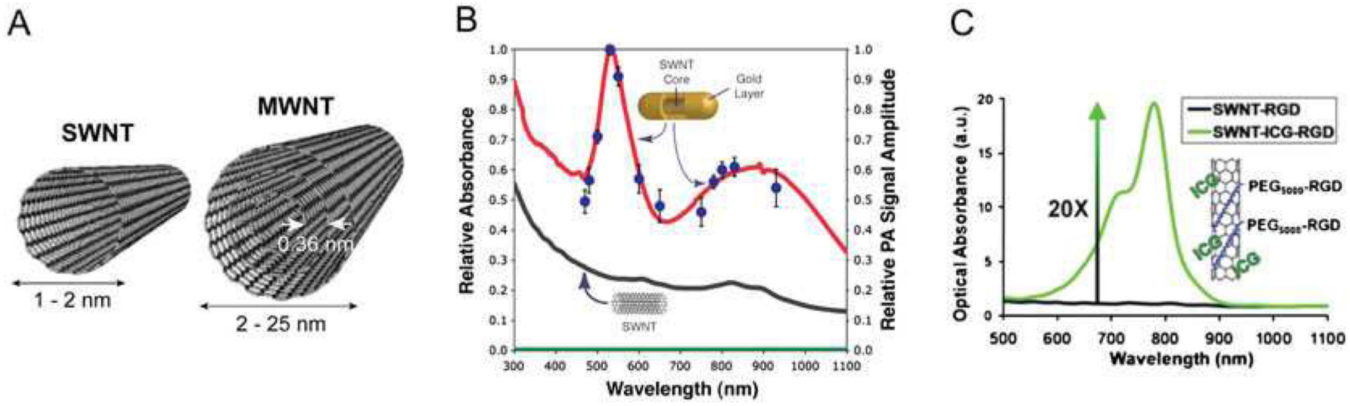

Figure 7.

(A) Schematic of single-walled and multi-walled carbon nanotubes (SWNT and MWNT, respectively). (B) Absorption spectra of SWNTs and golden carbon nanotubes (GNTs), and photoacoustic (PA) spectra of GNTs. Lines represent normalized optical spectra (left vertical axis) of GNTs in water (red curve), SWNTs in water (black curve) and water only (green curve) and the dots represent normalized PA signal amplitude (blue dots, right axis) of GNTs in water. The concentration of the SWNTs is ~35 times higher than that of GNTs; hence 85- to 100-fold enhanced NIR contrast is achieved by the hybrid GNTs. Reproduced with permission from Kim et. al. (36). (C) Optical absorption spectrum of SWNT-RGD (black curve) and indocyanine green-enhanced SWNT-RDG (SWNT-ICG-RGD, green curve). The optical absorbance spectrum of plain SWNT-RGD is relatively flat with slight gradual absorption decrease as the wavelength increase. However, by attaching a large number of ICG molecules to the SWNT surface, a 20-fold increase in optical absorption results at 780 nm. Reproduced with permission from de la Zerda et. al. (34)

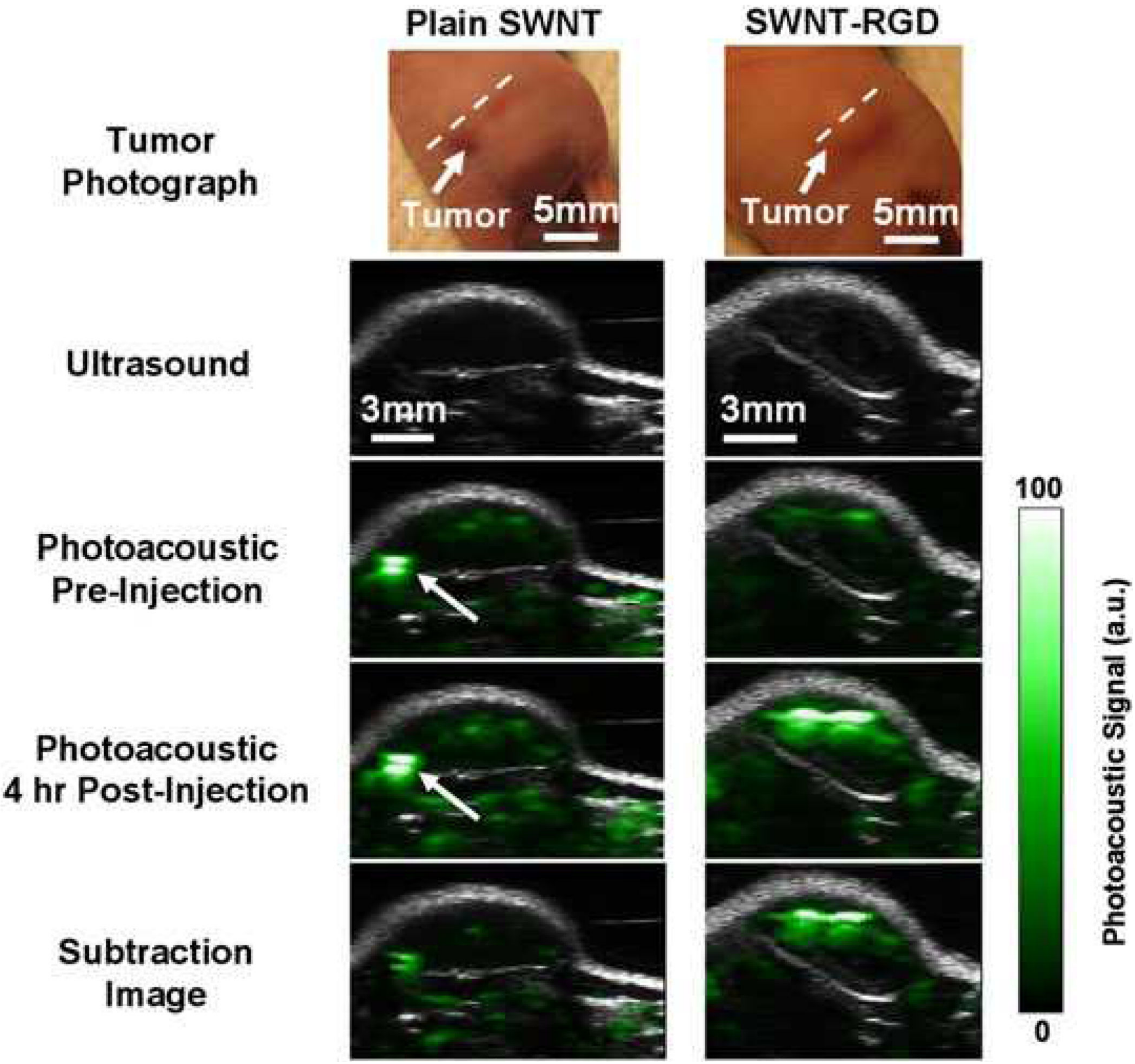

Figure 8.

Single-walled carbon nanotube argine-glyice-aspartic acid (SWNT-RGD) tumor targeting in living mice. Ultrasound (gray) and photoacoustic (PA) (green) images of a vertical slice (white dotted line) through the tumors of mice injected with SWNT-RGD (right column) and control plain SWNTs (left column). Subtraction images were calculated as 4 h post-injection minus pre-injection to remove tissue background signal from the PA image. Mice injected with SWNT-RGD showed an averaged 7-fold PA signal increase in the tumor over mice injected with control untargeted SWNTs. The high PA signal in the mouse injected with plain SWNTs (indicated by the white arrow) is not seen in the subtraction image, suggesting that it is due to a large blood vessel and not SWNTs. Reproduced with permission from de la Zerda et. al. (52)

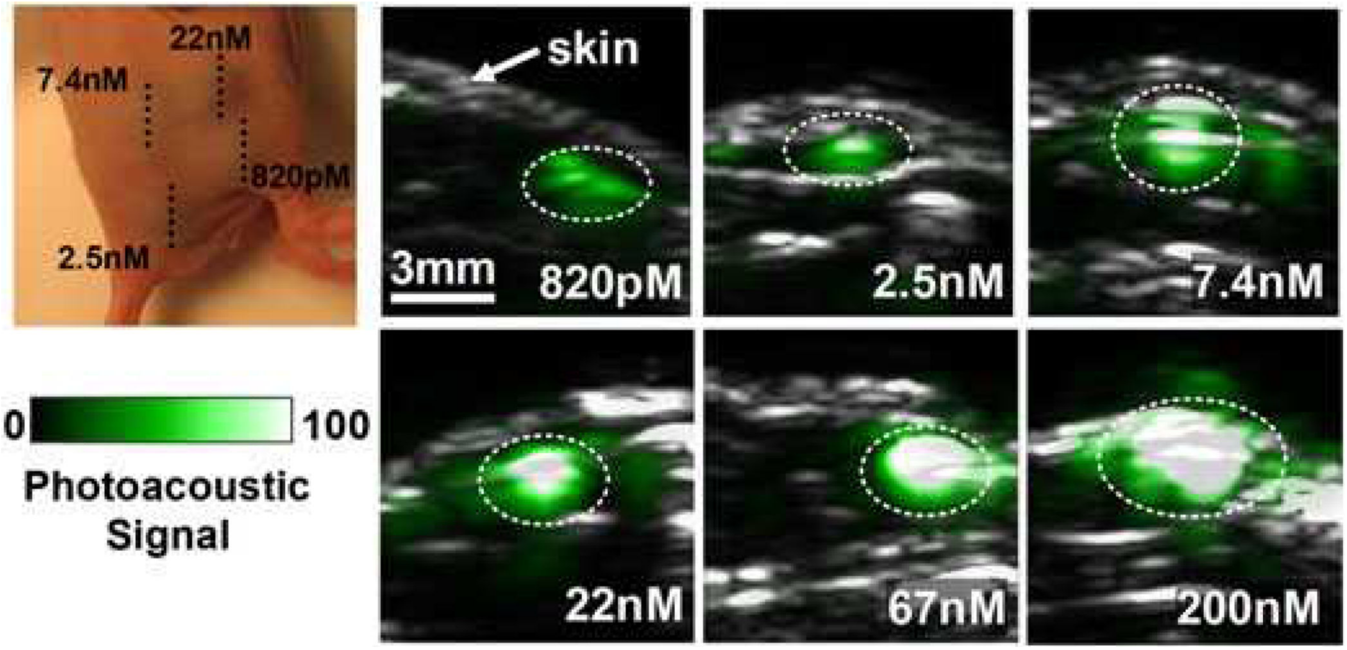

Figure 9.

Photoacoustic (PA) detection of single-walled carbon nanotube indocyanine green (SWNT-ICG) in living mice. Vertical slices of ultrasound images (gray) and PA images (green) of mice injected subcutaneously with SWNT-ICG-RGD at concentrations of 0.82–200 nm (dotted black line). The white dotted lines on the images illustrate the approximate edges of each inclusion. Quantitative analysis of the images estimated that 170 pm of SWNT-ICG-RGD gives the equivalent PA signal as the tissue background. Reproduced with permission from de la Zerda et. al. (34)

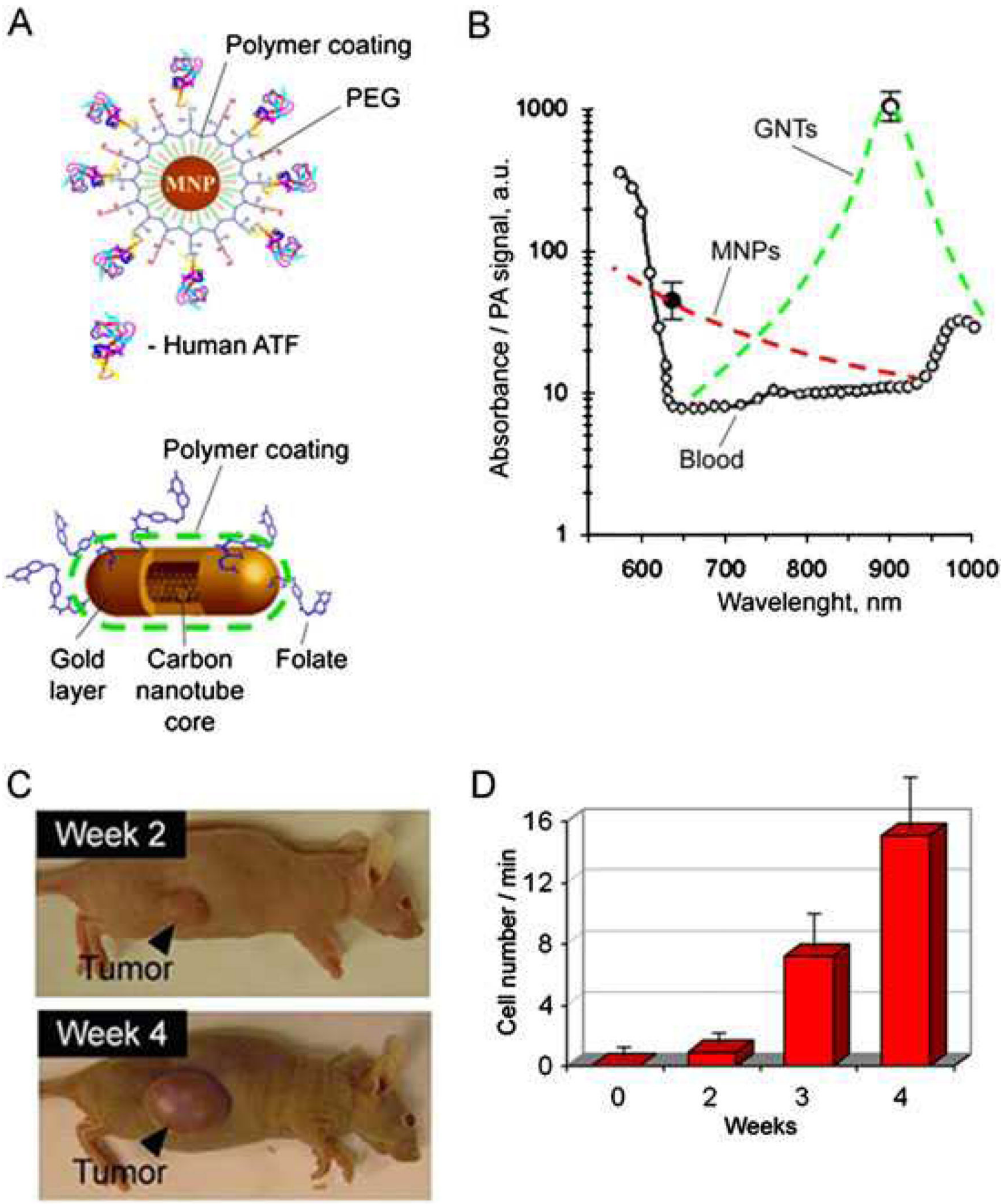

Figure 10.

In vivo multiplex two-color photoacoustic (PA) detection of circulating tumor cells (CTCs). (A) The 10 nm magnetic NPs (MNPs) coated with amphiphilic triblock polymers, polyethylene glycol (PEG) and the amino-terminal fragment of urokinase plasminogen activator (ATF). The 12 × 98 nm GNTs coated with PEG and folic acid. (B) PA spectra of ~ 70μm veins in mouse ear (open circles). Absorption spectra of the MNPs and GNTs (dashed curves) normalized to PA signals from CTC labeled with MNPs (black cricle) and GNTs (open circle). (C) The size of the primary breast cancer xenografts at different time stages of tumor development. (D) Average rate of CTCs in mouse ear vein. Reproduced with permission from Galanzha et. al. (35)

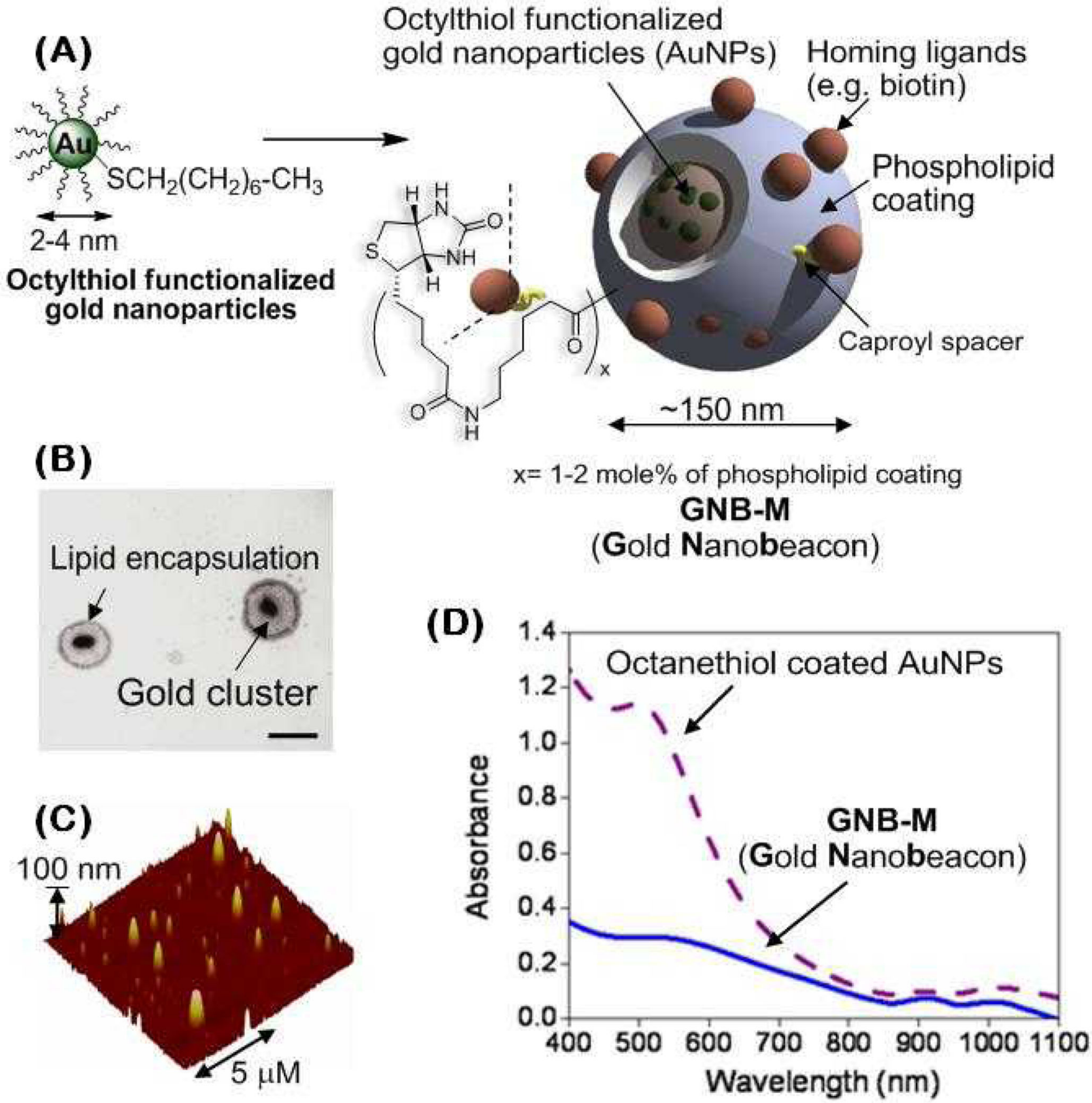

Figure 11.

(A) Preparation of gold nanobeacons from octanethiol-functionalized gold nanoparticles (AuNPs). x=1–2 mol% phospholipid coating. (B) TEM image of gold nanobeacons (drop deposited over nickel grid, 1% uranyl acetate; scale bar: 100 nm). (C) AFM image of gold nanobeacons. Average height H_{av}/nm=(10151) nm. (D) UV/Vis spectroscopic profile. Solid blue line: gold nanobeacons; purple dashed line: octanethiol-coated AuNPs. Spectra are not normalized. [Reproduced with permission from ref. 53]

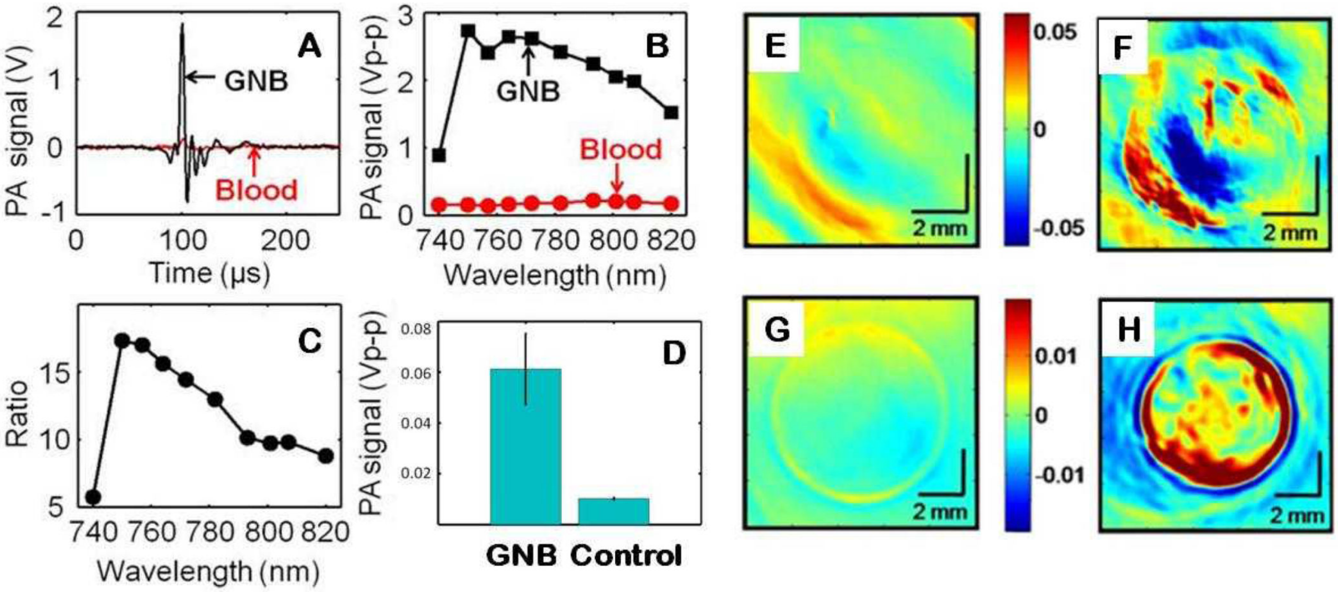

Figure 12.

(A) PA signals generated from a Tygon® tube (I.D. 250 μm, O.D. 500 μm) filled with GNB and rat blood. The excitation light is of 764 nm wavelength. (B) PA spectrum of GNB and blood over a 740–820 nm range of NIR wavelengths. (C) Ratio of the peak-to-peak PA signal amplitudes generated from GNB to those of blood. (D) PA signal to noise ratio for the GNB and the control (no gold). Cross-sectional PA image of a low density polyethylene (LDPE) tube (~1cc volume, I.D. ~6 mm) filled with plasma clot: (E) control, (F) targeted with GNB using a curved array PA system (λ = 800 nm). (G) Control, (H) targeted with GNB using a photoacoustic breast scanner system (λ = 532 nm). [Reproduced with permission from ref. 53]

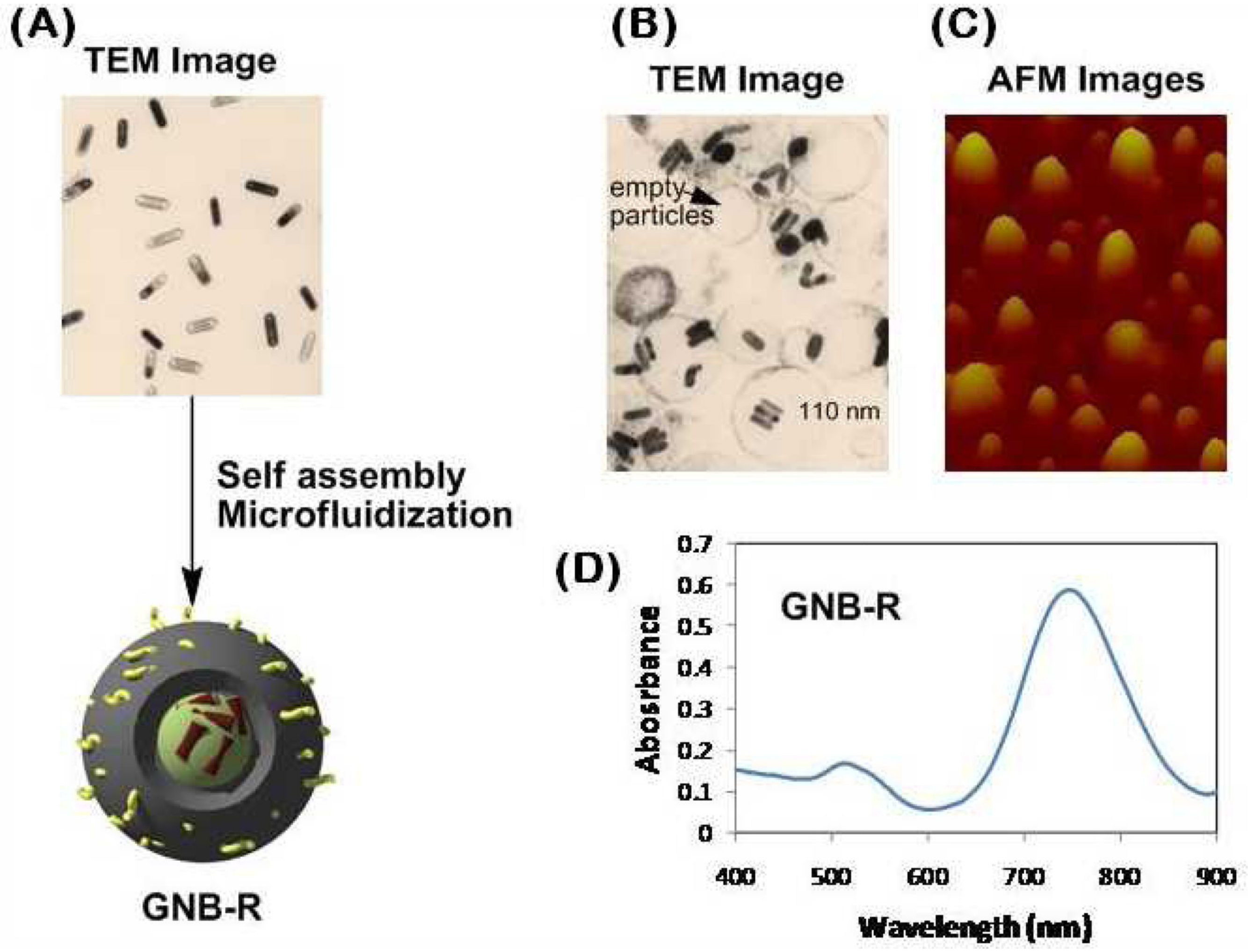

Figure 13.

(A) TEM image of gold nanorods drop deposited over Ni-grid; (B) TEM images of GNB_R drop deposited over Ni-grid; (C) AFM images of GNB_R drop deposited over glass; (D) UV-vis spectrum of gold nanorods showing LSPR and TSPR bands at 750 nm and 530 nm respectively. [Reproduced with permission from ref. 55]

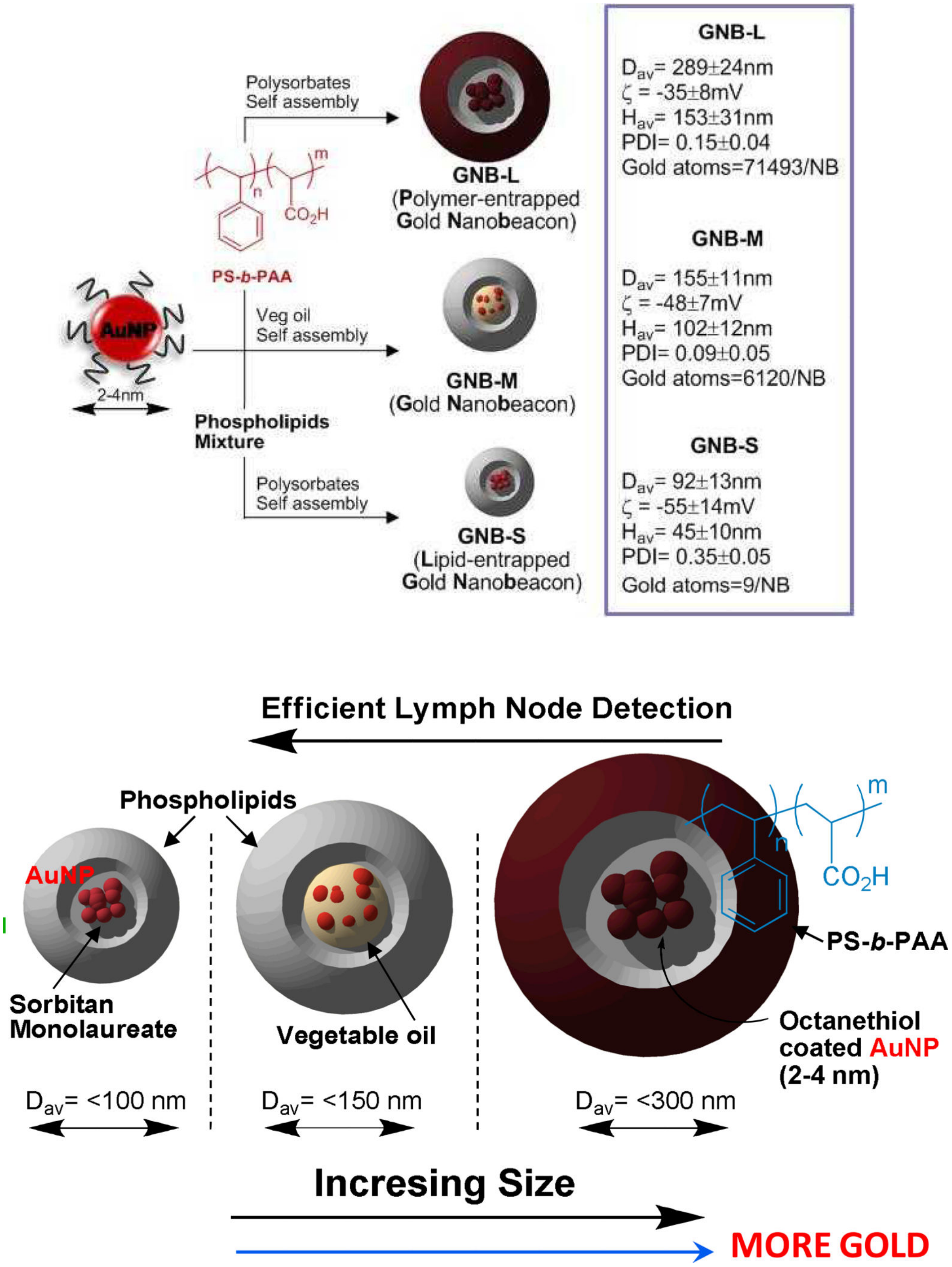

Figure 14.

Top: Synthesis of GNBs. (D_{av} = Number averaged (DLS); ζ = electrophoretic (zeta) potential; H_{av} = average height (AFM); PDI = polydispersity index (DLS)). Bottom: a general scheme showing the effect of particle size in facile lymphatic distribution. [Reproduced with permission from ref. 54]

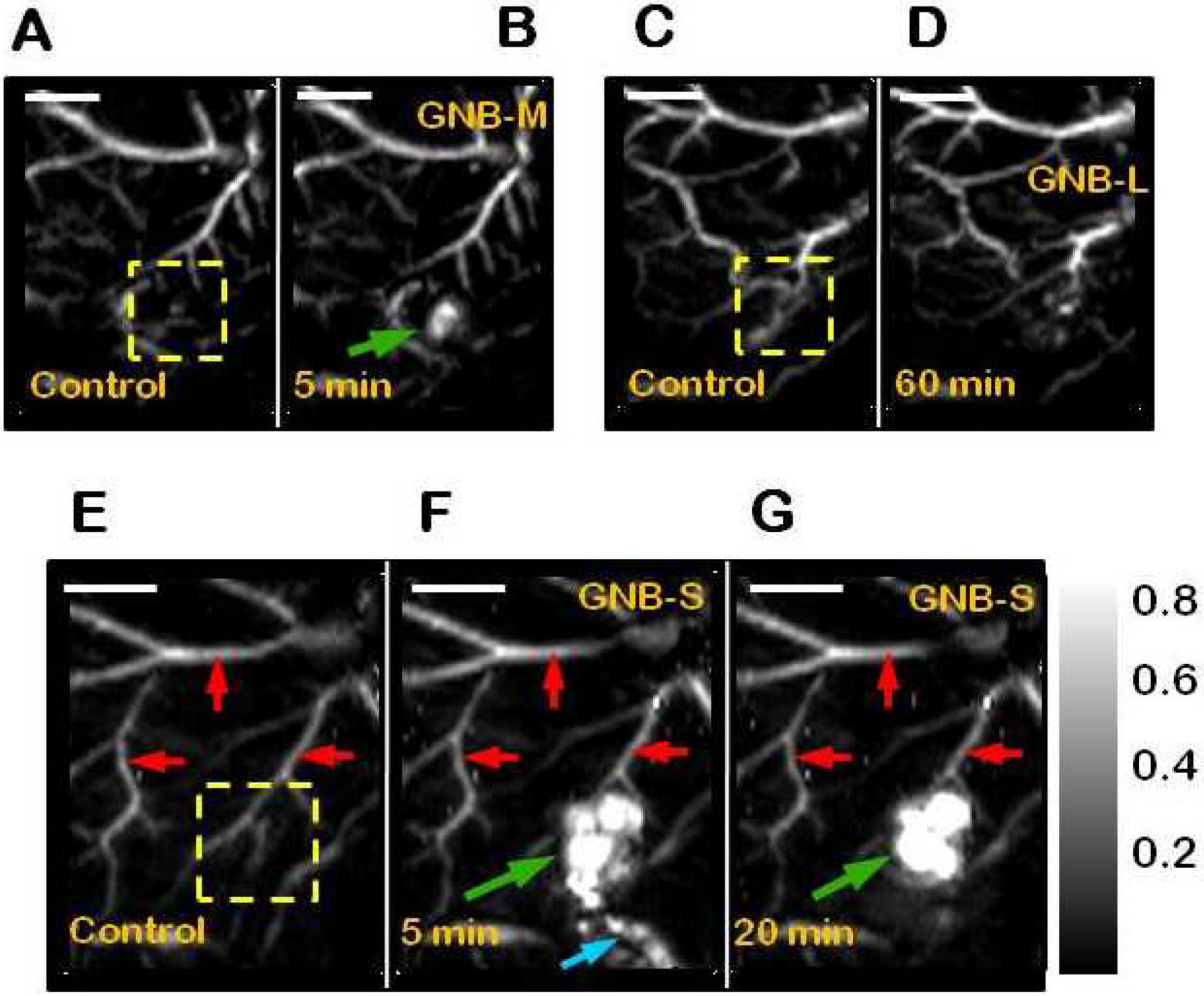

Figure 15.

In vivo noninvasive photoacoustic imaging of sentinel lymph nodes in rat (λ=767 nm). (A–G) Scale bar is 5mm. 150 mL of nanobeacons were injected intradermally in all the cases. GNB_1: (A). Control PA image. (B) 5 min post-injection image of GNB_1 (5 mM). GNB_P: (C). Control PA image. (D). Lymph node is not visible in a 60 min postinjection image of GNB_P (680 nM). GNB_S: (E). Sagittal maximum amplitude projection (MAP) [67] pre-injection control image: Bright parts represent optical absorption from blood vessels, marked with red arrows. (F). PA image (MAP) acquired 5 min after GNB_S injection (10 nM). SLNs are clearly visible, marked with green arrow. Lymphatic vessel is also visible, marked with blue arrow. (G). 20 min post-injection PA image. [Reproduced with permission from ref. 54]

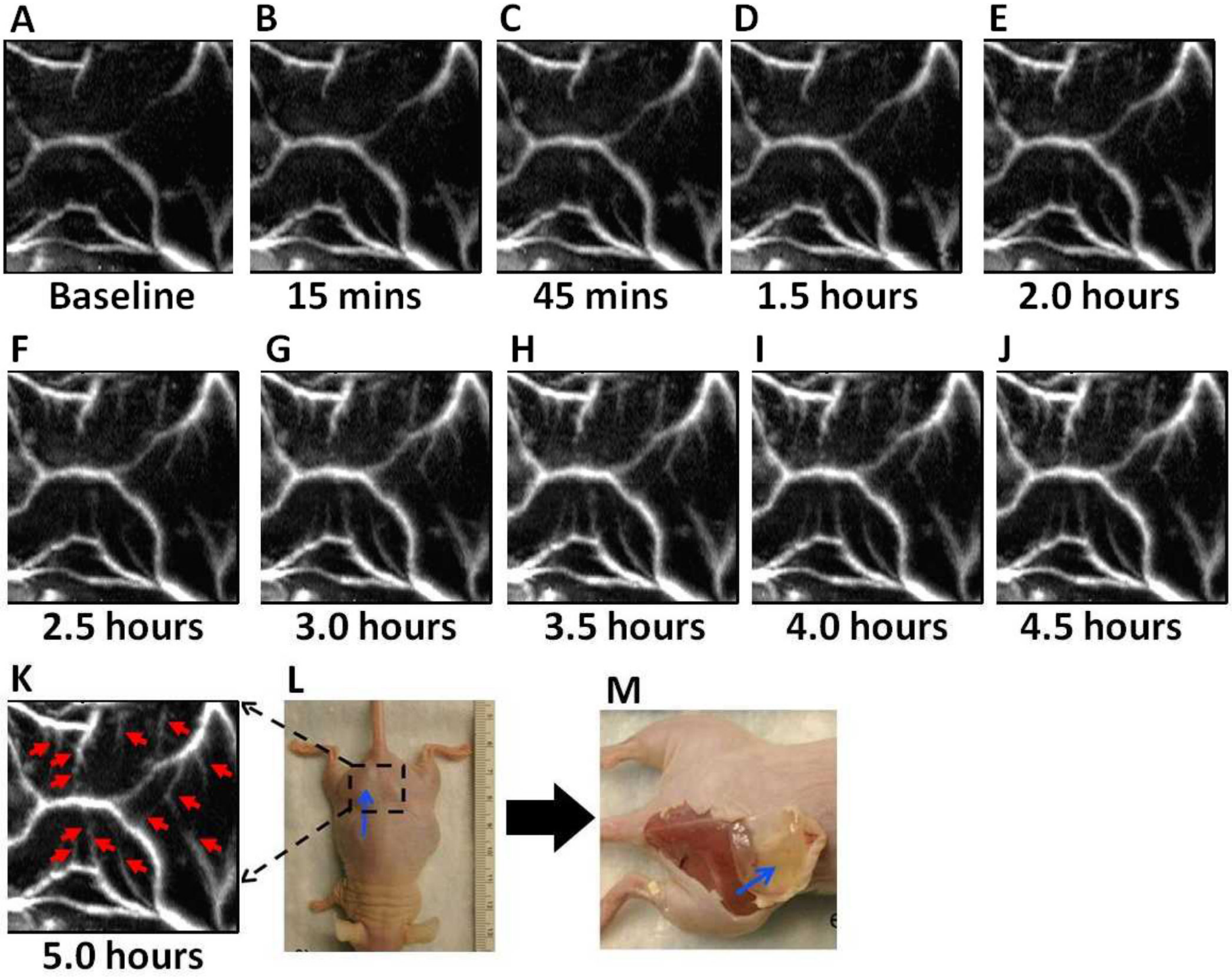

Figure 16.

0.75 mL of Matrigel™ was implanted subcutaneously in nude mouse. The mouse was imaged photoacoustically 8–20 days after Matrigel™ implantation. (A) Photoacoustic (PA) maximum amplitude projection (MAP) image of the dotted area. This is a control image. After the control image was taken targeted gold nanobeacons ($\alpha_v\beta_3$-GNB-M) were injected intravenously using the tail vein. In a time course study (B–K), PA images were acquired with an interval of approximately 1/2 hour up to 5 h. (G) Three hour post-injection PA image. Red arrows point to the angiogenic sprout (not visible in A). (K) Five hour post-injection PA image. For all PA images λ = 767 nm, scale bar = 5 mm. (L) Digital photograph of a mouse implanted with Matrigel™ plug. Blue arrow points to the plug. The black dotted area was imaged. The smallest tick: 1 mm. (M) Digital photograph of the sacrificed mouse after all the image acquisition was over. The skin was removed to show the Matrigel™ plug (blue arrow). [Reproduced with permission from ref. 56]

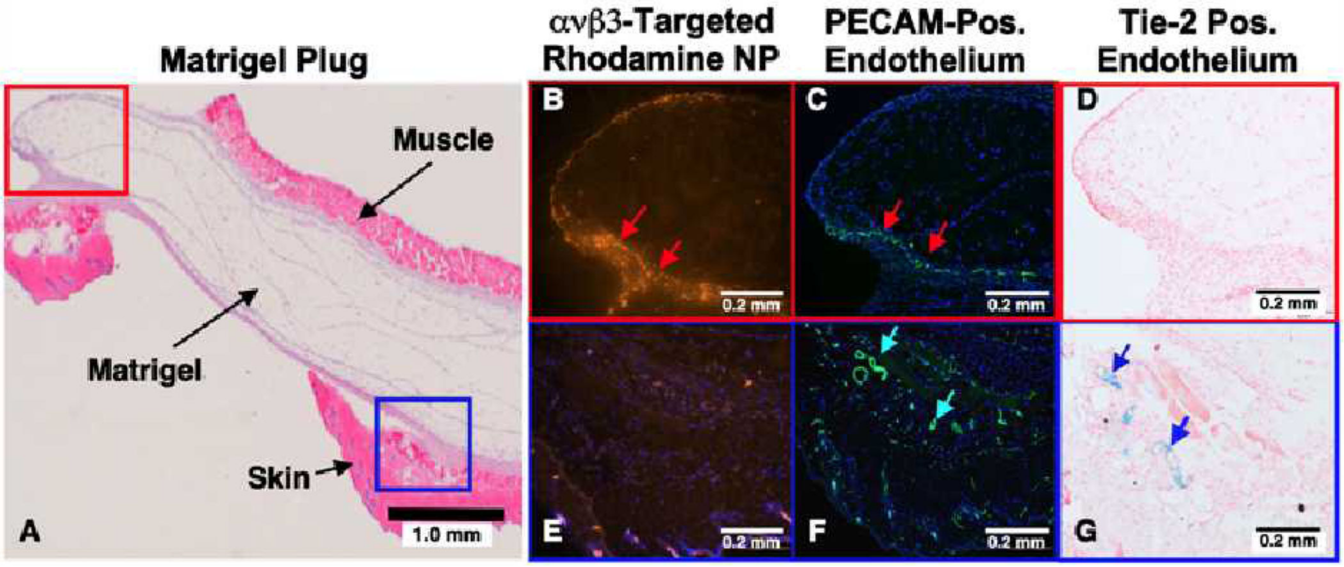

Figure 17.

Microscopic examination of FGF Matrigel subcutaneous explant from FVB/N-TgN(TIE2LacZ)182Sato mice following injection (IV) of $\alpha_v\beta_3$-targeted rhodamine labelled GNB-M nanoparticles. These transgenic mice carry a beta-galactosidase reporter gene under the control of the murine Tek (Tie2) promoter. LacZ is expressed specifically in vascular endothelial cells in embryonic and adult mice. (A) H&E staining of the excised implant providing spatial orientation of the matrix with respect to skin and muscle. The red box region is further examined in figures B, C and D. The blue box region is studied in more detail in panels E, F, and G. Panels B and E depict the accumulation of $\alpha_v\beta_3$-targeted rhodamine nanoparticles in the red and blue tissue regions respectively. Note the brilliant and dense accumulation of NPs in panel B (red arrows) and little to no accumulation of particles in the panel E. Region. Panels C and F depict the staining of vascular endothelium for PECAM (CD34) in the red (C) and blue (F) regions of the matrigel plug. There was dense vascularity in both locations (Red arrows in C and turquoise arrows in F. Panels D and G depict the LacZ signal for betagalactosidase under Tie2 promoter control. In panel D, no LacZ signal was appreciated, reflecting a paucity of mature microvessels. In contradistinction, there is strong LacZ signal in panel G. These results indicated that the $\alpha_v\beta_3$-GNB nanoparticles were specifically targeted to angiogenic endothelial cells (PECAM + /Tie-2 −) and not to more mature microvessels, which were PECAM +, Tie-2 +. The data corroborated that PAT imaging with $\alpha_v\beta_3$-targeted GNB specifically distinguished and enhanced the angiogenic neovasculature from new, but more matured and differentiated microvessels. [Reproduced with permission from ref. 56]

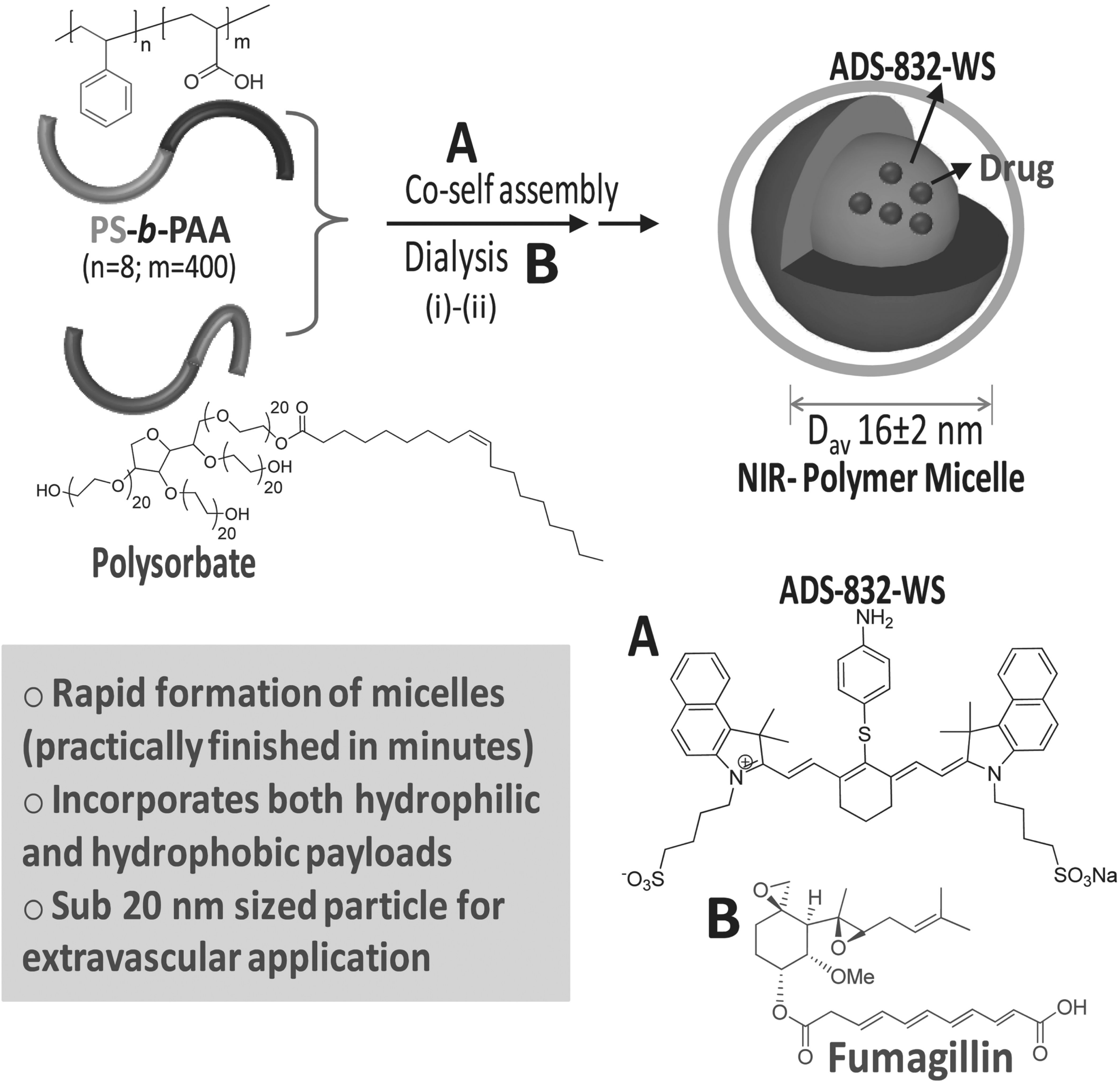

Figure 18.

Synthesis and characterization of theranostic polymeric micelles: i) co-self assembly of amphiphilic diblock copolymer and sorbitan monooleate, ADS-832-WS (A) and/or fumagillin (B), sonication, 25°C, 1 min; ii) dialysis 10 kDa cellulosic membrane, nanopure water (0.2 μM). Reproduced with permission from Pan. et. al. (98)

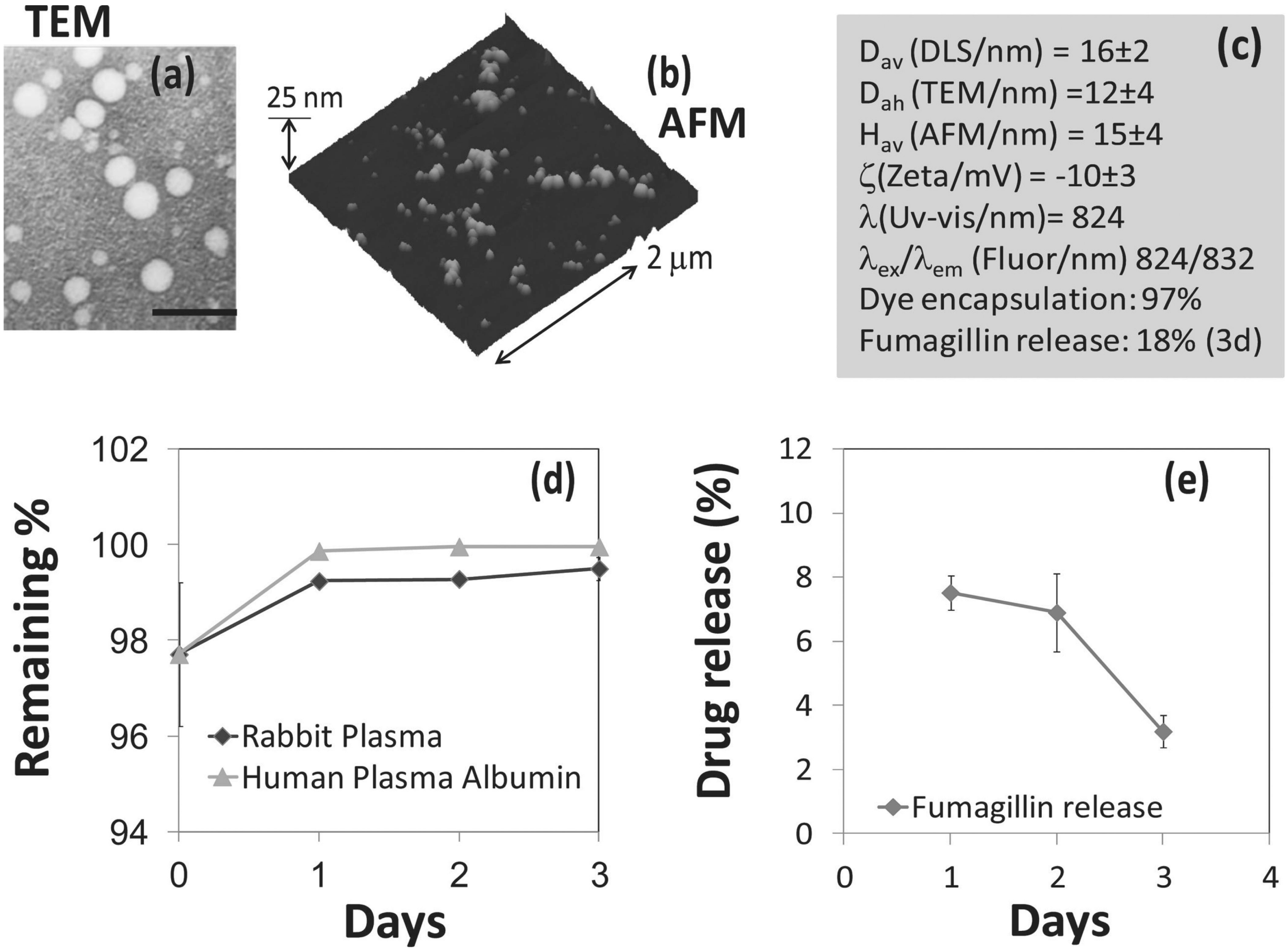

D_{av} (DLS/nm) = 16±2
D_{ah} (TEM/nm) =12±4
H_{av} (AFM/nm) = 15±4
ζ(Zeta/mV) = -10±3
λ(Uv-vis/nm)= 824
$\lambda_{ex}/\lambda_{em}$ (Fluor/nm) 824/832
Dye encapsulation: 97%
Fumagillin release: 18% (3d)

Figure 19.

a) TEM image of the polymeric micelles drop desposited over nickel brid, scale bar = 100 nm; b) AFM image of the micelles drop deposited over glass; c) physiochemical characterization table for a NIR-polymer micelle; d) dissolution of ADS-832-WS from micelle when incubated against rabbit plasma and human plasma albumin; (e) time-dependent release of fumagillin from micelle. Reproduced with permission from Pan. et. al. (98)

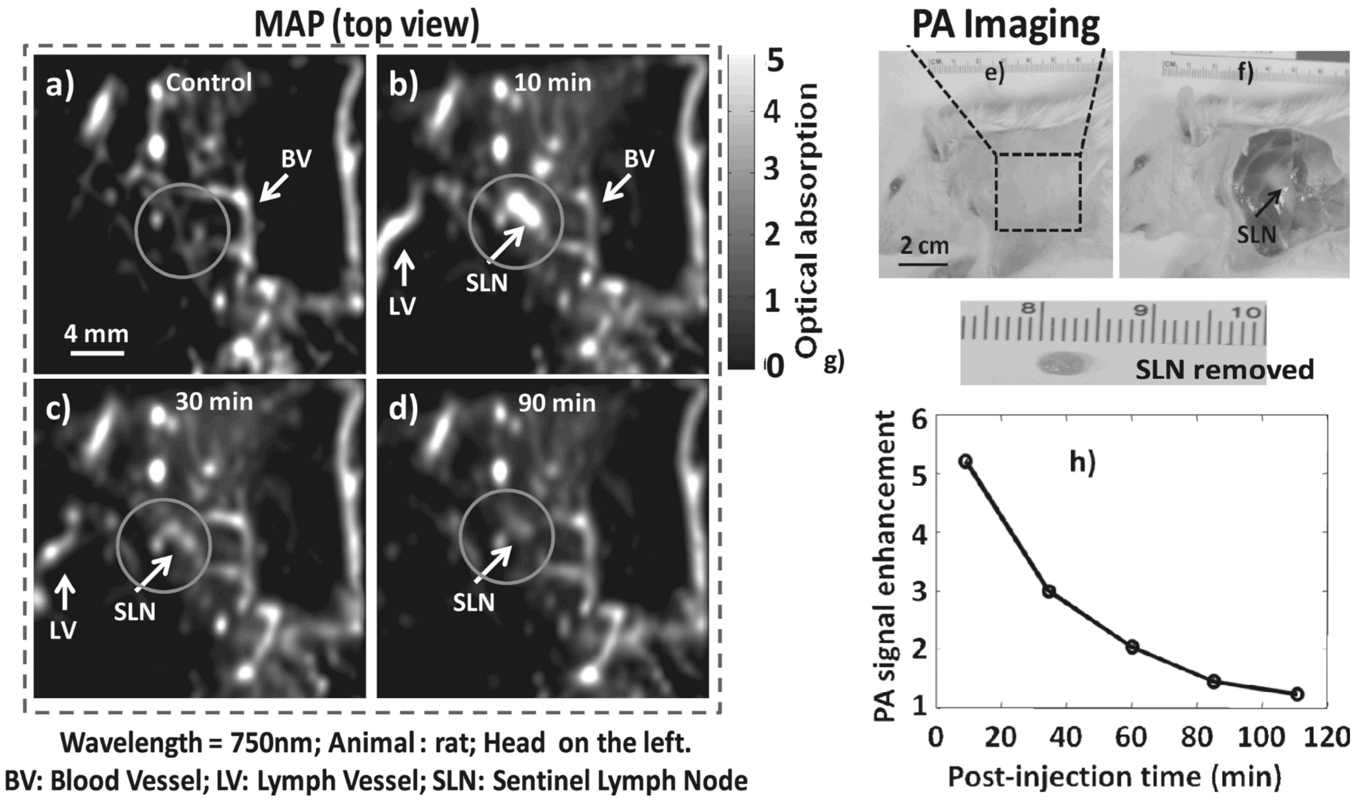

Figure 20.

Non-invasive in vivo PA images of SLN in rat: For all PA images, the laser was tuned to 750 nm wavelength. a) Control PA image acquired before polymeric nanoparticle injection. Bright parts represent optical absorption, here, from blood vessels (BV). b) PA image (MAP) acquired immediately after the polymeric nanoparticle injection. c) 35 min post-injection PA image. d) 110 min post-injection PA imageBlood vessel (BV), lymph vessel (LV) and sentinel lymph node (SLN) are marked with arrows, and the SLN is visible in (b)–(d), however, invisible in (a). e) Photograph of the rat after the hair was removed from the scanning region before taking the PA images. The scanning region is marked with a black dotted square. f) Photograph of the rat with the skin removed after PA imaging. g) Excised lymph node. Smallest tick: 1 mm. h) PA signal enhancement in the SLN after the injection of polymeric nanoparticle as a function of post-injection time. For (a)–(d): FOV = 25 mm × 24 mm, step size along the X direction = 0.2 mm, step size along the Y direction = 0.4 mm, total scan time = − 23 min. No signal averaging was used. Reproduced with permission from Pan. et. al. (98)

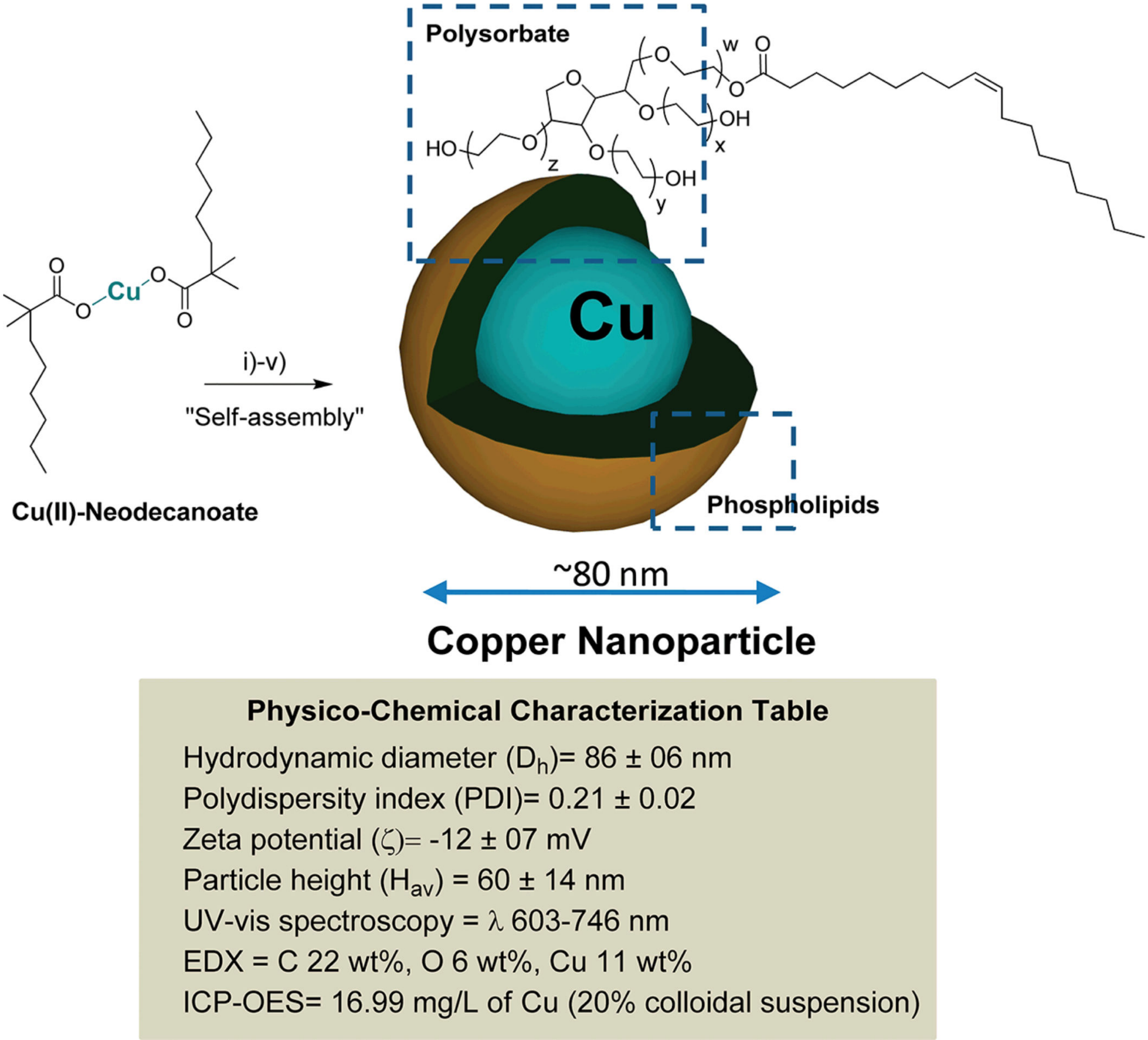

Physico-Chemical Characterization Table

Hydrodynamic diameter (D_h)= 86 ± 06 nm
Polydispersity index (PDI)= 0.21 ± 0.02
Zeta potential (ζ)= -12 ± 07 mV
Particle height (H_{av}) = 60 ± 14 nm
UV-vis spectroscopy = λ 603-746 nm
EDX = C 22 wt%, O 6 wt%, Cu 11 wt%
ICP-OES= 16.99 mg/L of Cu (20% colloidal suspension)

Figure 21.

Synthesis and physiochemical characterization of self-assembled nanoparticles of copper neodecanoate. Schematic describing the preparation of copper-enriched nanoparticles: (i) suspension of copper neodecanoate (1) in sorbitan sesquioleate, vigorously vortex and mixing, filter using cotton bed, vortex; (ii) dissolve phospholipids in anhydrous chloroform and preparation of phospholipid thin film by slow evaporation of solvent at 45°C under reduced pressure; (iii) resuspension of the thin film in water (0.2 μM); (iv) self-assembly by high pressure homogenization at 4°C, 20000 psi (141 MPa), 4 min; (v) dialysis (cellulosic membrane, MWCO 20k); in box, characterization table for nanoparticles of copper neodecanoate. Reproduced with permission from Pan et. al. (99)

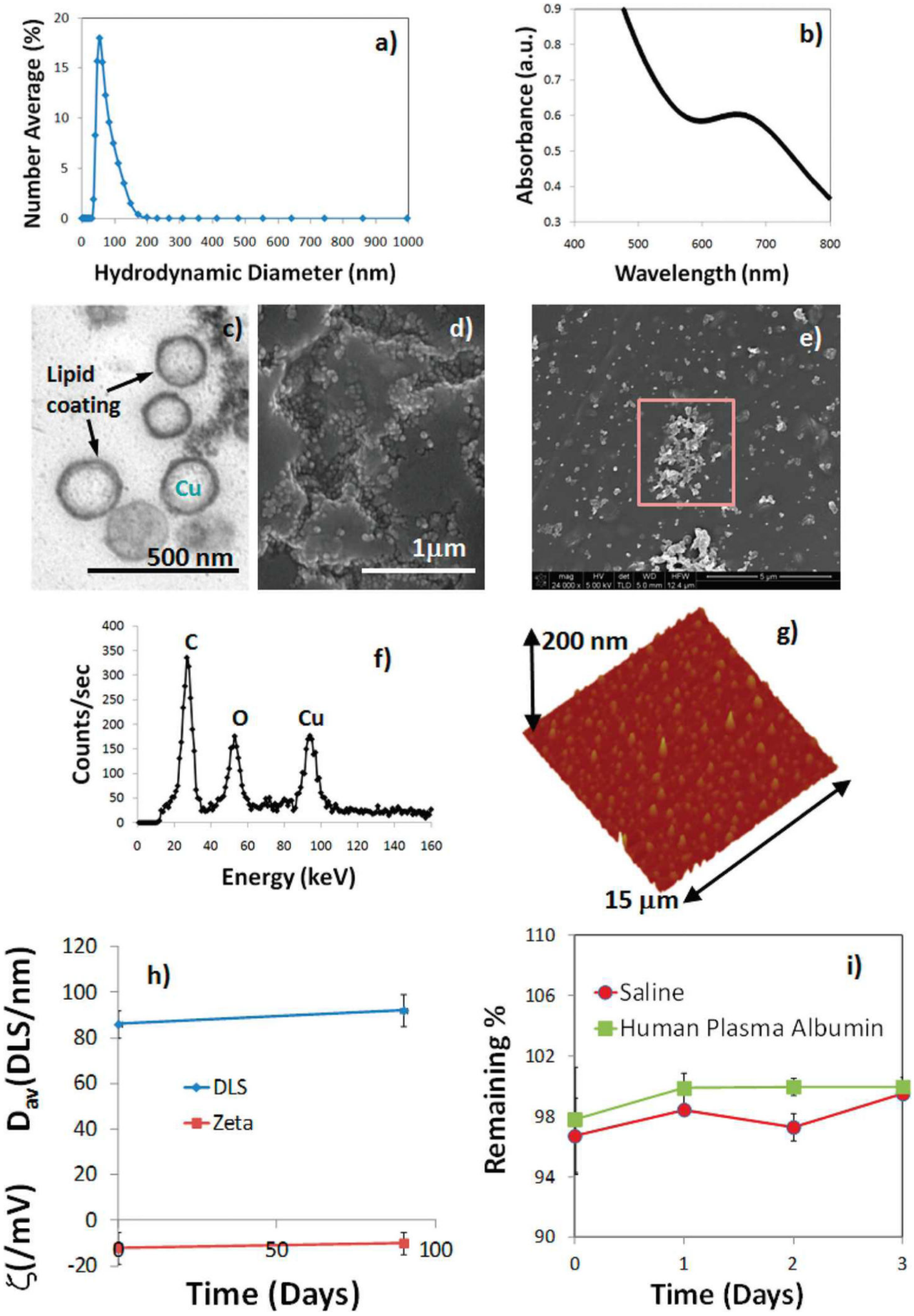

Figure 22.

Hydrodynamic particle size distribution from DLS; (b) UV-vis spectrum of NanoCuN nanoparticles in water; (c) anhydrous state TEM image; (d,e) SEM images; (f) EDX spectrum of the selected area from the image in (e); (g) AFM image (deposited on glass substrate); shelf life stability of NanoCuN over 90 days from formulation; (i) dissolution of Cu over 3 days when incubated with saline and human plasma albumin.

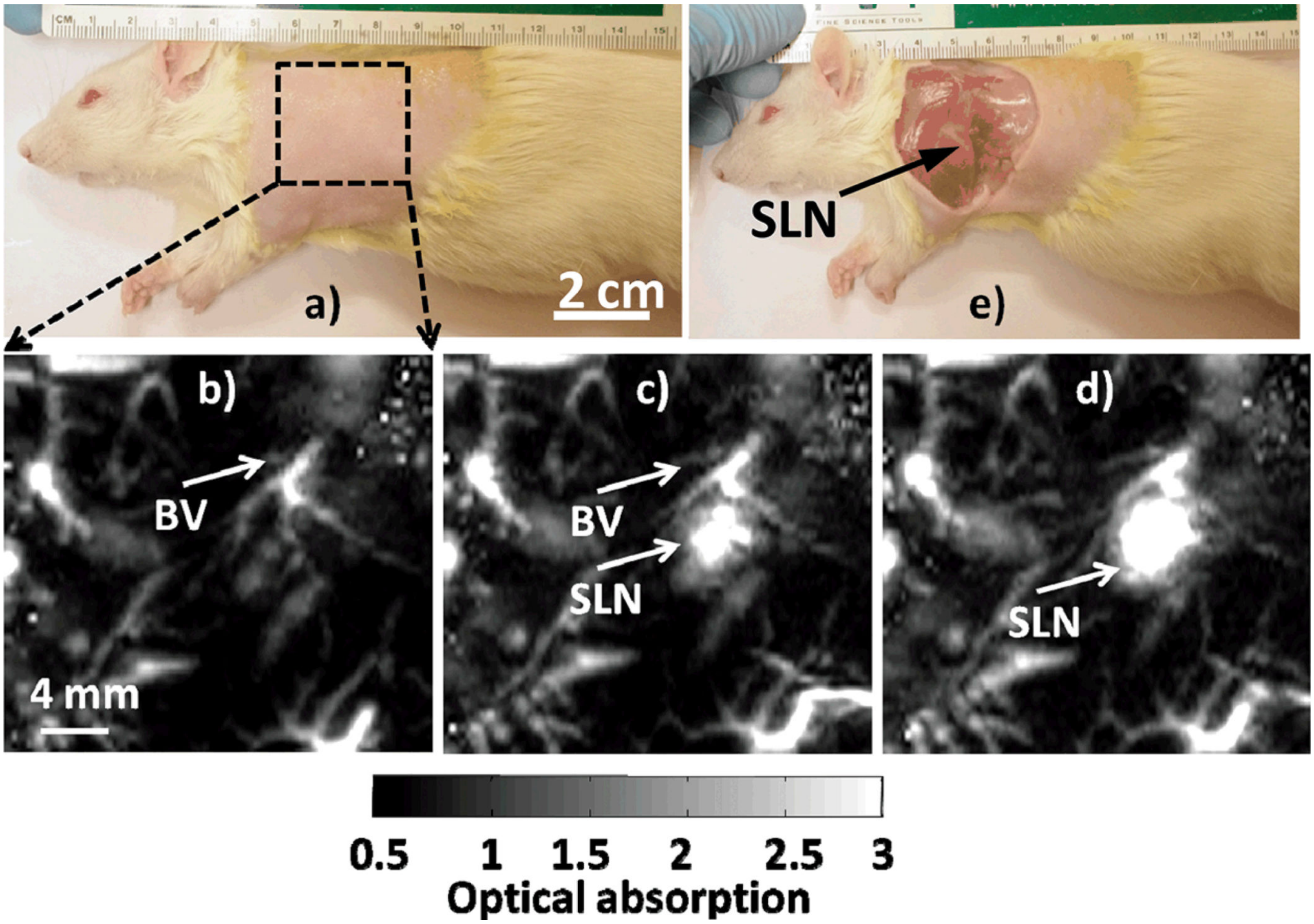

Figure 23.

Noninvasive in vivo PA images (maximum intensity projections, MIP) of the SLN in a rat. (a) Photograph of the rat with region of interest depilated before scanning. The scanning region is delineated by a black dotted square. (b) Baseline PA image acquired before NanoCuN injection. Bright regions represent inherent optical absorption from a blood vessel (BV). (c) PA image (MIP) acquired almost immediately after NanoCuN administration. (d) PA image 60 min post injection showing a marked signal enhancement corresponding to increased NanoCuN uptake by the node: Blood vessel (BV) and sentinel lymph node (SLN) are marked with arrows. The SLN is visible in both (c) and (d), however not apparent in (b). (e) Photograph of the rat with the skin excised after PA imaging. For (b)–(d), FOV = 25 mm × 24 mm, step size along the X direction = 0.2 mm, step size along the Y direction = 0.4 mm, total scan time = ~ 23 min. No signal averaging was used. Reproduced with permission from Pan et. al. (99).

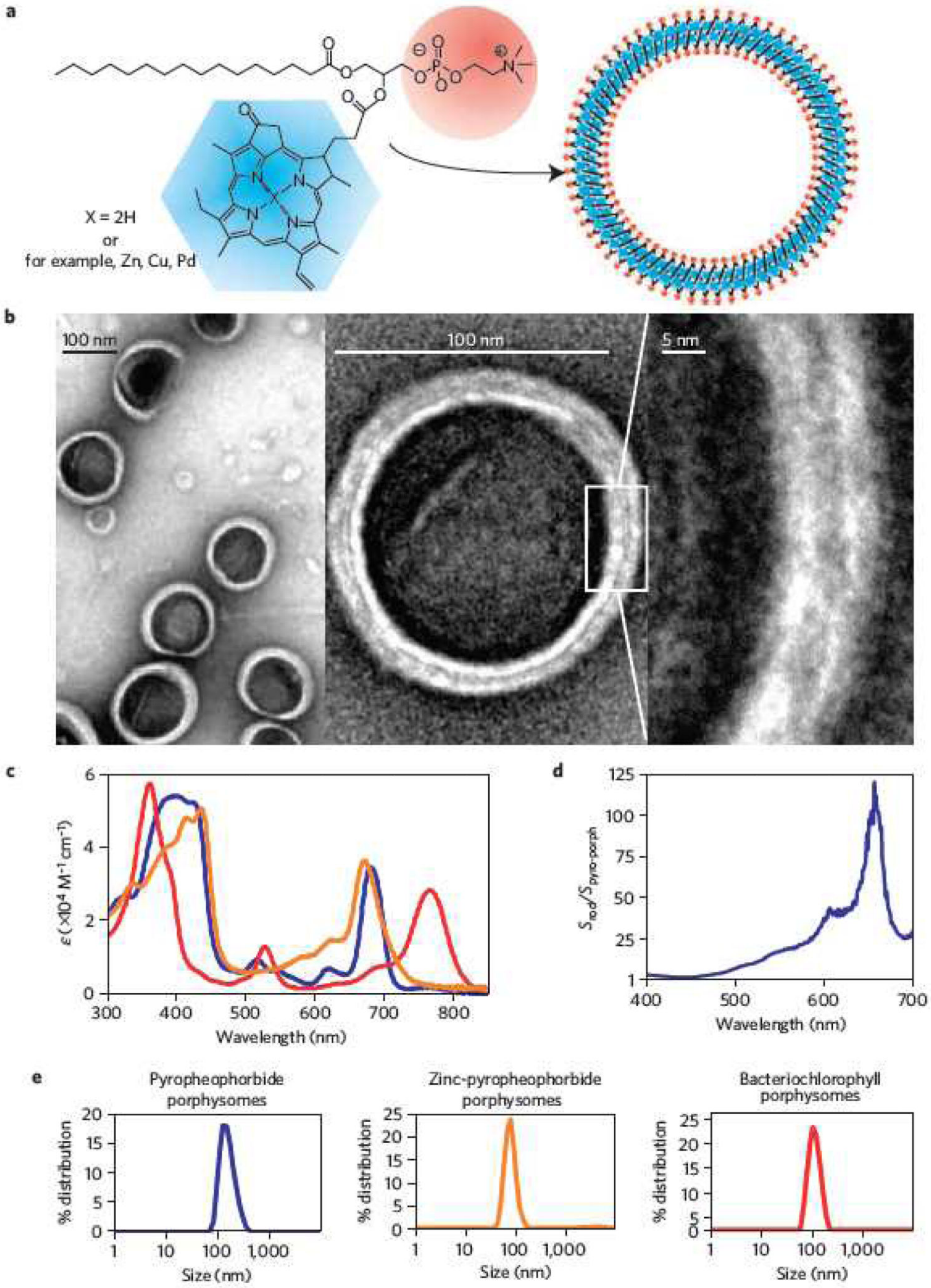

Figure 24.

Porphysomes are optically active nanovesicles formed from porphyrin bilayers. a, Schematic representation of a pyropheophorbide–lipid porphysome. The phospholipid headgroup (red) and porphyrin (blue) are highlighted in the subunit (left) and assembled nanovesicle (right). b, Electron micrographs of negatively stained porphysomes (5% PEG-lipid, 95% pyropheophorbide-lipid). c, Absorbance of the porphyrin–lipid subunits incorporated in porphysomes formed from pyropheophorbide (blue), zinc pyropheophorbide (orange) and bacteriochlorophyll (red) in PBS. d, Resonance light scattering spectra ratio between gold nanorods and pyropheophorbide porphysomes. Nanorod and porphysome concentration was adjusted to have equal optical density at 680 nm. e, Dynamic light scattering size profiles of indicated porphysomes recorded in PBS. Reproduced with permission from Lovell et. al. (109)

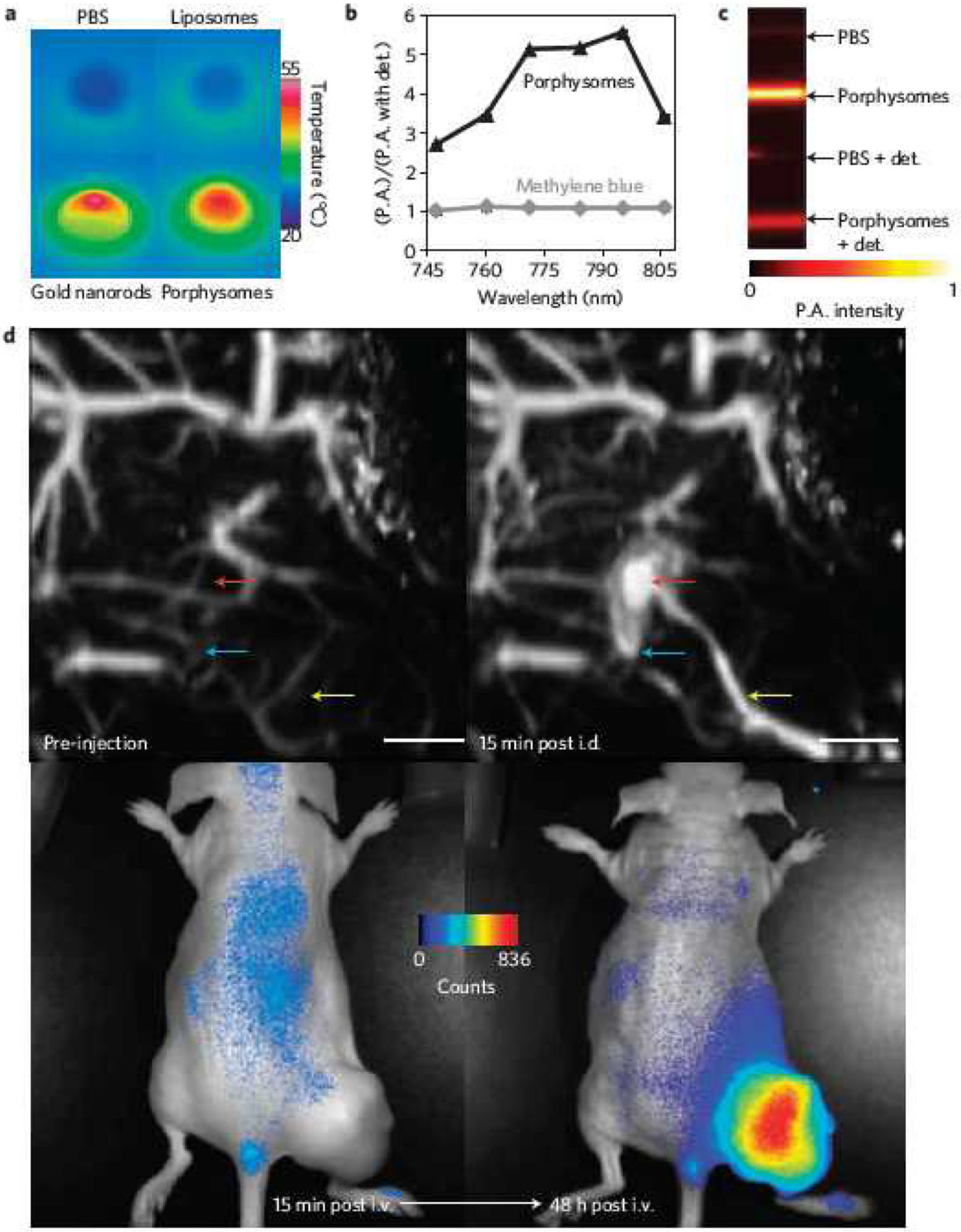

Figure 25.

Multimodal optical utility of porphysomes. **a**, Photothermal transduction. Solutions were irradiated with a 673nm laser and imaged with a thermal camera. **b**, Ratio of photoacoustic amplitudes (P.A.) measured for porphysomes and methylene blue ±0.5% Triton X-100 (mean ± s.e.m. from 10 measurements). det., detergent. **c**, Photoacoustic images of tubing containing porphysomes and PBS measured ±0.5% Triton X-100. **d**, Dual modality for photoacoustic contrast and activatable fluorescence. Top, lymphatic mapping. Rats were imaged using photoacoustic tomography before and after intradermal (i.d.) injection of porphysomes (2.3 pmol). Secondary lymph vessels (cyan), lymph node (red), inflowing lymph vessel (yellow) and 5mm scale bar are indicated. Bottom, fluorescence activation after i.v. injection of porphysomes (7.5 pmol) in a KB xenograft-bearing mouse. Reproduced with permission from Lovell et. al. (109)